JEM Journal of Experimental Medicine

ARTICLE

Prenatally derived macrophages support choroidal health and decline in age-related macular degeneration

Seth D. Fortmann[1,2], Blake F. Frey[1,3], Robert F. Rosencrans[1,2], Yvonne Adu-Rutledge[2], Edgar Ready V[2], Kameron V. Kilchrist[4], Robert S. Welner[5], Michael E. Boulton[2], Daniel R. Saban[6], and Maria B. Grant[2]

Hallmark findings in age-related macular degeneration (AMD) include the accumulation of extracellular lipid and vasodegeneration of the choriocapillaris. Choroidal inflammation has long been associated with AMD, but little is known about the immune landscape of the human choroid. Using 3D multiplex immunofluorescence, single-cell RNA sequencing, and flow cytometry, we unravel the cellular composition and spatial organization of the human choroid and the immune cells within it. We identify two populations of choroidal macrophages with distinct FOLR2 expression that account for the majority of myeloid cells. FOLR2⁺ macrophages predominate in the nondiseased eye, express lipid-handling machinery, uptake lipoprotein particles, and contain high amounts of lipid. In AMD, FOLR2⁺ macrophages are decreased in number and exhibit dysfunctional lipoprotein metabolism. In mice, FOLR2⁺ macrophages are negative for the postnatal fate-reporter *Ms4a3*, and their depletion causes an accelerated AMD-like phenotype. Our results show that prenatally derived resident macrophages decline in AMD and are implicated in multiple hallmark functions known to be compromised in the disease.

Introduction

Photoreceptors are among the most metabolically demanding cells in the body (Hoang et al., 2002; Pan et al., 2021). They require vast inputs of glucose, lipid, and oxygen for phototransduction and produce equally large outputs of lipidic and proteinaceous waste through outer segment shedding (Ames et al., 1992; Joyal et al., 2016; Okawa et al., 2008; Young, 1971). The choroid is the dense, fenestrated vascular bed that supplies the photoreceptors with nutrients and facilitates the systemic removal of waste products (Lejoyeux et al., 2022). In humans, the choroid is nearly equal in thickness to that of the neural retina (Liu et al., 2023), and it is separated from the photoreceptors by a single monolayer of cells, called the retinal pigmented epithelium (RPE). Accordingly, the RPE and choroid have coevolved extreme measures to match the metabolic needs of photoreceptors. The choroid has the greatest blood flow per gram of any tissue (Alm and Bill, 1972), and a single RPE cell ingests a daily lipid load equivalent to that of a hepatocyte (Reyes-Reveles et al., 2017). Over the lifespan of certain individuals, these processes can gradually deteriorate, leading to the development of age-related macular degeneration (AMD).

AMD is an insidious disease of aging that primarily affects individuals in their seventh and eighth decades of life, and it is the leading cause of vision loss in older adults (Wong et al., 2014). The hallmark finding of AMD is drusen, which is the accumulation of extracellular lipoprotein debris in the membranous space between the RPE and choroid, known as Bruch's membrane (Curcio et al., 2011). Additional features include vasodegeneration of the choriocapillaris, choroidal neovascularization (CNV), fibrosis, and ultimately neurodegeneration of central vision photoreceptors (Curcio et al., 2011; Jia et al., 2014; Lutty et al., 2020; McLeod et al., 2009; Mullins et al., 2011).

40 years ago, Sarks and colleagues identified chronic inflammation within the choroid as a ubiquitous feature of AMD pathology (Penfold et al., 1984). Using electron microscopy, they observed abundant immune cells at sites of drusen deposition, including mononuclear phagocytes (MPs), lymphocytes, and mast cells (Penfold et al., 1984). MPs were uniquely enriched in and around drusen, where they appeared to phagocytose and breakdown the deposits, often while in direct contact with nearby lymphocytes (Killingsworth et al., 1990; Penfold et al.,

[1]Medical Scientist Training Program (MSTP), University of Alabama at Birmingham (UAB), Birmingham, AL, USA; [2]Department of Ophthalmology, UAB, Birmingham, AL, USA; [3]Department of Pathology, UAB, Birmingham, AL, USA; [4]Discovery Medicine, Kodiak Sciences, Inc., Palo Alto, CA, USA; [5]Division of Hematology/Oncology, Department of Medicine, UAB, Birmingham, AL, USA; [6]Department of Ophthalmology, Duke University, Durham, NC, USA.

Correspondence to Maria B. Grant: mariagrant@uabmc.edu; Seth D. Fortmann: sfortma2@uab.edu

M.B. Grant is a lead contact.

1984, 1985). Soon thereafter, immunohistochemistry directed against MHC class II (MHCII) confirmed the presence of MPs within the nondiseased human choroid and introduced the hypothesis that these cells may be of dendritic lineage (Baudouin et al., 1988). Follow-up work in AMD donor eyes demonstrated an enrichment of MPs in CNV lesions and a depletion of these cells in areas of atrophy (Cherepanoff et al., 2010; McLeod et al., 2016). In AMD, choroidal MPs appear to undergo a phenotypic shift that includes reduced size, loss of ramified processes, and increased expression of iNOS (Cherepanoff et al., 2010; Killingsworth et al., 1990; McLeod et al., 2016; Penfold et al., 1984). More recently, single-cell RNA sequencing (scRNA-seq) has shed new light on the immune landscape of the human choroid, with abundant MPs, lymphocytes, and less frequent mast cells being recovered (Collin et al., 2023; Voigt et al., 2019, 2020, 2022). Yet, debate persists regarding, among others, the classification of choroidal MPs (macrophage versus dendritic and subtypes thereof), the role of these cells in the pathogenesis of AMD, and the existence of lymphocytes in the human choroid (McMenamin et al., 2019; Wu et al., 2024). To date, there has not been a comprehensive investigation of human choroidal immune cells using gold-standard techniques like flow cytometry.

Due to this paucity of human data, most of what is known about choroidal MPs in AMD comes from mice. However, murine ocular anatomy challenges extrapolation to humans as mice lack the central macula fundamental to AMD and have rudimentary, hypoplastic choroids that are only 15–20% of the thickness of the neural retina (Yang et al., 2020). Nonetheless, the laser-induced CNV mouse model (Lambert et al., 2013) has proven useful in studying choroidal angiogenesis and in predicting the clinical efficacy of anti–vascular endothelial growth factor (VEGF) treatments in neovascular AMD (Heier et al., 2012; Saishin et al., 2003). In this system, choroidal MPs are widely considered proangiogenic by migrating to sites of laser injury within the choroid and promoting the growth of new vessels (Espinosa-Heidmann et al., 2003; Sakurai et al., 2003). These proangiogenic MPs express CD11c (Droho et al., 2023) and are mostly derived from circulating CCR2^{+} monocytes (Sennlaub et al., 2013; Tan et al., 2016; Tsutsumi et al., 2003). Conversely, a homeostatic role for choroidal MPs is less clear. In a live imaging study using CX3CR1 fluorescent reporter mice, choroidal MPs were found lining the posterior portion of the choriocapillaris and appeared to constitutively phagocytose debris by extending long, dynamic processes to the basal interface of Bruch's membrane. In another study, chronic global depletion of macrophages using a small molecule inhibitor resulted in progressive choroidal degeneration (Yang et al., 2020), and genetic deletion of CCL2 or its cognate receptor CCR2 resulted in lipid accumulation and choroidal dysfunction (Ambati et al., 2003). These findings suggest that choroidal MPs may be beneficial to the health and maintenance of the choroid. However, given the limitations of mouse ocular anatomy and the unknowns of the human choroid, it remains unclear to what degree immune cells of the mouse choroid reflect that of our own. Accordingly, the role of human choroidal MPs in health and AMD remains incompletely understood. To this end, an understanding of the immune repertoire of the human choroid, how it changes in AMD, and how it relates to that of the murine eye are of critical importance. Herein, we use a variety of existing and newly developed methods to demonstrate that the human choroid contains a dense and diverse array of immune cells. We show, among others, that a previously unknown prenatally derived macrophage is uniquely involved in lipid metabolism and vascular maintenance and is decreased in the choroids of AMD donors. In mice, targeted depletion of this population recapitulates key features of AMD pathology.

Results

Cellular composition and spatial organization of the human choroid

The human choroid is inherently challenging to study given that it is heavily pigmented, highly autofluorescent, and anatomically obscured between thick, dense scleral collagen posteriorly and pigmented, autofluorescent RPE anteriorly (McLeod and Lutty, 1994). To circumvent these challenges, we developed a 3D multiplex immunofluorescence method that allows for the simultaneous detection of 30+ markers on centimeter-scale choroidal whole mounts. This approach involves removing the sclera and RPE, depigmentation, autofluorescence quenching, and antigen retrieval, followed by cyclic rounds of immunostaining, confocal imaging, and fluorophore bleaching (Fig. S1). The resulting images are then stitched, registered, and stacked using computational methods to create a 3D multiplexed model of the human choroid. We used this method, in conjunction with scRNA-seq, to construct a comprehensive mapping of the cellular composition and spatial organization of the human choroid.

To guide the identification of distinct cell populations, we created an atlas of human choroidal scRNA-seq data derived from seven publicly available datasets (GSE203499, GSE230348, GSE210543, GSE135922, GSE149100, GSE183320, GSE202735), which included 99 unique samples across 64 total donors (51 macular donors and 46 peripheral donors) (Collin et al., 2023; Mullin et al., 2023; Voigt et al., 2019, 2020, 2022). After preprocessing, quality control filtering, and dimensionality reduction, 178,920 total cells were recovered spanning six major cell types: endothelium, pericytes/smooth muscle, melanocytes, fibroblasts, Schwann cells, and immune cells (Fig. 1 A). We then identified unique marker genes for each cluster (Fig. 1 B) and used antibodies to these markers to discriminate the six populations with 3D multiplex immunofluorescence (Fig. 1 C).

Using our 3D multiplex immunofluorescence method, endothelium stained with UEA-lectin, displayed classic spatial organization, with posteriorly positioned larger vessels (outlined in white) giving rise to the dense choriocapillaris located anteriorly (Fig. 1 C; orange). Smooth muscle actin (SMA) marked contractile mesenchymal cells, including pericytes and smooth muscle cells, which were found exclusively on larger caliber vessels and were in the greatest density along arterioles (Fig. 1 C; yellow). Melanocytes, stained by melan-A (MLANA), were located posterior to the choriocapillaris and were densely packed in the spaces between the larger caliber vessels, which constituted the true, extravascular parenchyma of the choroid

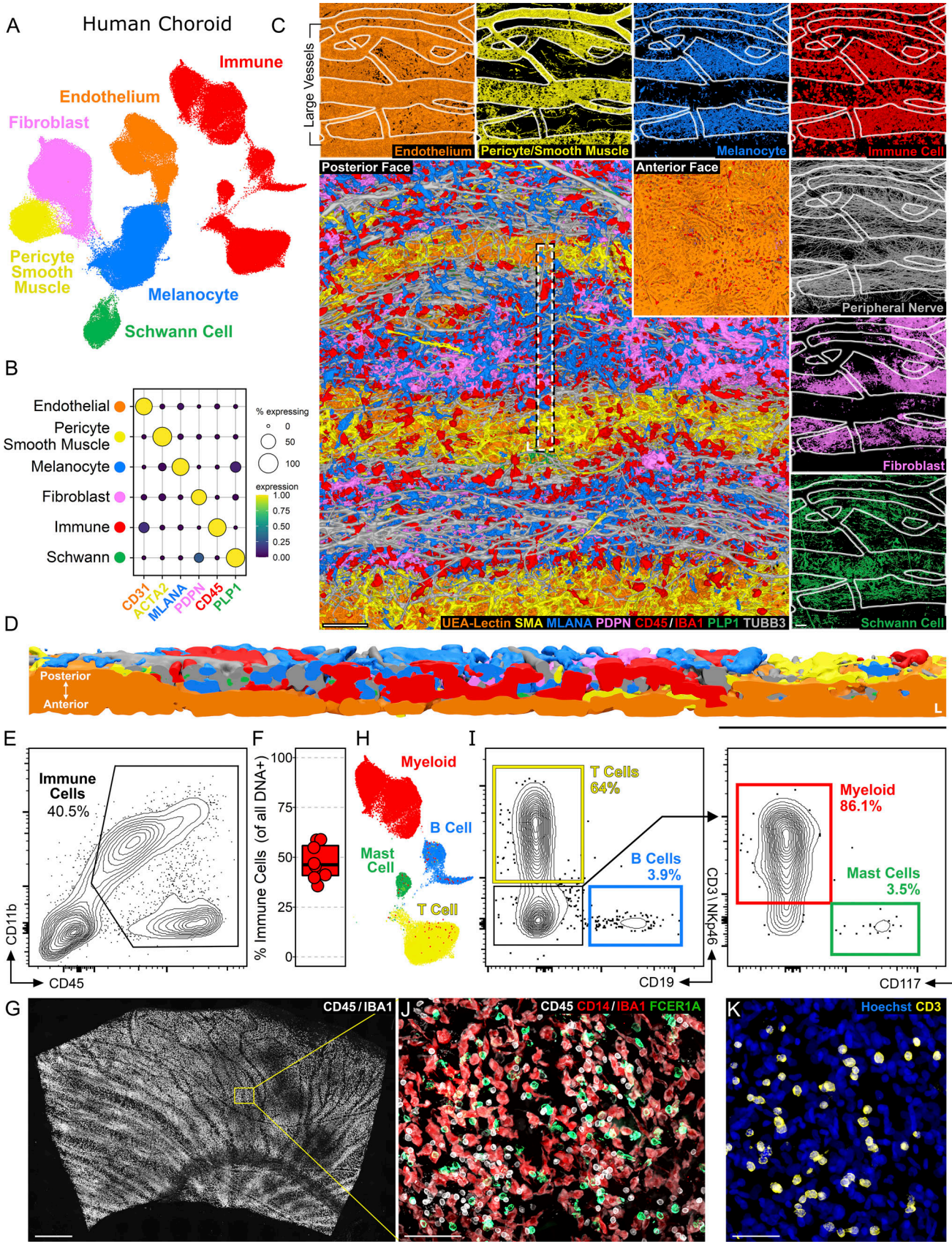

Figure 1. **Spatial organization and cellular composition of the human choroid. (A)** UMAP of scRNA-seq data from the choroids of 64 individuals. **(B)** scRNA-seq marker genes of the six clusters from A. **(C)** Multiplex immunofluorescence of a human peripheral choroid showing the six cell populations from

A plus TUBB3 for peripheral nerves. 3D renderings are shown. Anterior (RPE-facing) and posterior planes are shown for the combined image. White outlined areas represent larger caliber vessels. Note that the majority of immune cells are extravascular and reside above the choriocapillaris and outside of the larger caliber vessels. Scale bars = 100 µm. **(D)** Transverse section of 3D rendering showing the area outlined with the white dashed rectangle from C. Note that the immune cells in red are extravascular. **(E)** Flow cytometry from a representative nondiseased donor showing immune cell gating on all live-nucleated cells. **(F)** Immune cell frequencies relative to all nucleated cells from nondiseased donors (n = 9 eyes) using flow cytometry. **(G)** CD45 channel from multiplex immunofluorescence showing immune cell distribution in peripheral choroid. Maximum intensity projection is shown. Scale bar = 1 mm. **(H)** UMAP of immune cells from scRNA-seq in A showing the overlaid expression of CD14 (red; myeloid), CD79A (blue; B cells), CD117 (green; mast cells), and CD3E (yellow; T cells). **(I)** Flow cytometry gating of the four immune cell populations shown in H. **(J)** Multiplex immunofluorescence of area bound by yellow box in G showing myeloid cells (CD14; red), mast cells (FCER1A; green), and pan immune marker (CD45; white). Maximum intensity projection is shown. Scale bar = 100 µm. **(K)** Immunofluorescence of a separate choroidal whole mount showing T cells (CD3; yellow) and nuclei (Hoechst; blue). Scale bar = 50 µm.

(Fig. 1 C; blue). Fibroblasts, marked by podoplanin (PDPN), were also located within the true parenchyma and showed similar spatial organization to that of melanocytes (Fig. 1 C; purple). Schwann cells, the smallest of the six clusters, were marked by proteolipid protein 1 (PLP1) and overlapped with a dense network of peripheral nerves stained with tubulin β-3 (TUBB3) (Fig. 1 C; green and gray, respectively). These nerves were located posterior to the choriocapillaris and were densest within the parenchyma, running alongside larger feeder vessels. Of note, choroidal nerves were absent from the scRNA-seq data because their cell bodies are located in the dorsal ganglia (Reiner et al., 2018). Lastly, immune cells, stained with CD45 and IBA1, appeared in high densities and varied widely in size and morphology (Fig. 1 C; red). Located immediately posterior to the choriocapillaris and in the spaces between the larger vessels, the immune cells were extravascular and populated the true parenchyma of the choroid (Fig. 1, C and D). These cells made many physical contacts, including with melanocytes and the outer surfaces of vessels, and were often adhered to choroidal nerves (Fig. 1, C and D). Given that the eye, and especially the posterior segment, have long been considered prototypical sites of immune privilege (Niederkorn and Stein-Streilein, 2010), it is intriguing that the choroid contains such high densities of extravasated immune cells.

In agreement with our 3D multiplex observations, the largest cell population within the human choroid per scRNA-seq was the immune cells, accounting for roughly one third of all cells. To further understand the immune landscape of the human choroid, we performed spectral flow cytometry on the digested choroids of nine nondiseased donor eyes (mean age 70 years; 80% male; Tables S1 and S2; and Fig. S2 A) and used CD11b and CD45 staining to gate on immune cells (Fig. 1 E; and Fig. S3, A and B). Relative to all nucleated (DNA^+) cells, choroidal immune cells had a median frequency of 46.3% ± 15% interquartile range (IQR) (Fig. 1 F). This remarkably high immune cell density can be appreciated across a large 10 × 6-mm piece of peripheral choroid stained with CD45 and IBA1 (Fig. 1 G).

Within the immune compartment of the human choroid, four discrete subpopulations were appreciated in the scRNA-seq data: myeloid cells, T cells, mast cells, and B cells (Fig. 1 H). T cells and myeloid cells were present in similar frequencies (46% and 40%, respectively) and accounted for the vast majority (86%) of all immune cells (Fig. 1 H). Using flow cytometry, we confirmed the presence of these four subpopulations of immune cells, and their frequencies were similar to that of the scRNA-seq data (Fig. 1 I). We used multiplex immunofluorescence to visualize the spatial organization of the different immune subpopulations within the human choroid (Fig. 1 J). Lymphocytes ($CD45^{++}$ $CD14^-$ $FCER1A^-$) appeared as small round cells, mast cells ($CD45^+$ $CD14^-$ $FCER1A^+$) were slightly larger spherical cells, and myeloid cells ($CD45^+$ $CD14^+$ $FCER1A^-$) were large and elongated in morphology (Fig. 1 J). Numerous immune interactions were noted, including between lymphocytes and myeloid cells, which appeared to make many physical contacts, likely representing antigen presentation (Fig. 1 J) to $CD3^+$ T cells (Fig. 1 K). In summary, our results reveal that the human choroid contains a dense array of immune cells, thereby implying that the posterior segment of the eye has a unique ability to maintain immune privilege despite an active and diverse immune repertoire.

Macrophages of the human choroid

We next focused on the myeloid compartment, and more specifically, the macrophages of the human choroid. Subclustering of the myeloid cells from the scRNA-seq data revealed seven different subpopulations: neutrophils, $CD1c^+$ conventional dendritic cells type 2, an indeterminate population with monocyte and macrophage-like features (monocyte/macrophage), two monocyte populations ($CD16^+$ monocytes and $CD14^+$ monocytes), and two large macrophage populations (folate receptor 2 $[FOLR2]^+$ macrophages and $FOLR2^-$ macrophages; Fig. 2 A and Fig. S3 C). The two macrophage populations, which lacked expression of known dendritic markers (Tirosh et al., 2016), accounted for roughly 64% of all myeloid cells and were distinguishable by the expression of FOLR2 and lymphatic vessel endothelial hyaluronan receptor 1 (LYVE1) versus CD11c and CD83 (Fig. 2 B). To confirm these two discrete macrophage types, we performed flow cytometry on choroidal digests from the aforementioned nine nondiseased human donor eyes. Within the $CD64^+$ $CD52^-$ macrophage gate (Fig. S3, A and B), we observed a large population of cells that stained brightly for FOLR2 and weakly for CD11c ($FOLR2^+$ macrophages) and a smaller population with the inverse staining pattern ($FOLR2^-$ macrophages; Fig. 2 C). Consistent with scRNA-seq (Fig. 2 B), mean fluorescent intensity analyses showed significantly higher LYVE1 staining and significantly lower CD83, CD45, and CD11b in the $FOLR2^+$ macrophages compared with the $FOLR2^-$ group (Fig. 2 D). FACS followed by live-cell imaging of the two macrophage populations revealed divergent morphologies (Fig. 2 E). $FOLR2^+$ macrophages had a larger, elongated shape with pseudopodia, while the $FOLR2^-$ macrophages were smaller and more spherical (Fig. 2 E). Multiplex immunofluorescence revealed similar morphological distinctions between the two

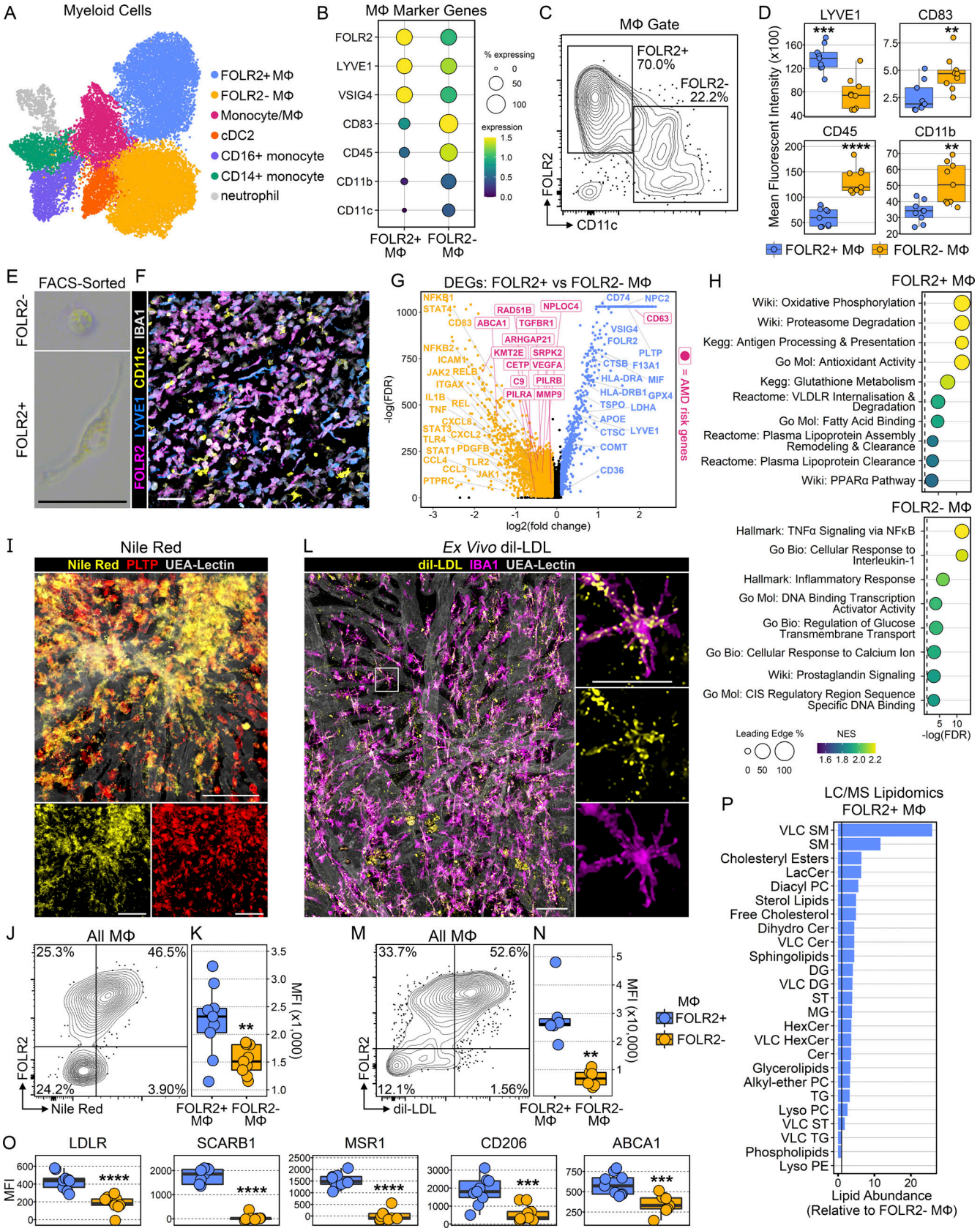

Figure 2. **Macrophage subpopulations in the human choroid. (A)** Subclustering of scRNA-seq data from myeloid cluster in (Fig. 1 I). UMAP plot is shown. **(B)** scRNA-seq marker genes of the two macrophage (MΦ) clusters from A. Log transformed, size factor normalized gene expression is shown. **(C)** Representative flow cytometry from a nondiseased donor pre-gated on macrophages showing the two macrophage subpopulations from A. **(D)** Flow cytometry

mean fluorescent intensities (MFIs) from FOLR2⁺ versus FOLR2⁻ macrophages. Four of the marker genes from B are shown. All donors were nondiseased (n = 9 eyes). Student's t test. **(E)** Live-cell imaging of FACS-sorted FOLR2⁻ and FOLR2⁺ macrophages from a nondiseased donor. Scale bar = 50 µm. **(F)** Multiplex immunofluorescence showing FOLR2⁻ and FOLR2⁺ macrophages. Scale bar = 50 µm. **(G)** Volcano plot of differentially expressed genes (DEGs) between FOLR2⁺ versus FOLR2⁻ macrophages from scRNA-seq data of nondiseased donors. Blue = genes upregulated in FOLR2⁺ macrophages (902 genes). Yellow = genes upregulated in FOLR2⁻ macrophages (3,762 genes). Magenta = AMD risk genes. **(H)** GSEA of DEGs from G showing selected pathways. Dashed lines represent significance cutoff. **(I)** Nile red staining in a choroidal whole mount from a nondiseased donor. Scale bar = 50 µm. **(J)** Representative flow cytometry plot from a nondiseased donor showing FOLR2 and Nile red staining in macrophages. **(K)** Flow cytometry MFI of Nile red staining in FOLR2⁺ and FOLR2⁻ macrophages. All donors were nondiseased (n = 9 eyes). Student's t test. **(L)** Representative immunofluorescence of human choroid incubated with dil-LDL. White box is area shown by magnified images to right. Large image scale bar = 100 µm. Small image scale bars = 50 µm. **(M)** Representative flow cytometry plot from a nondiseased donor showing FOLR2 and dil-LDL staining in macrophages. **(N)** Flow cytometry MFI of dil-LDL staining in FOLR2⁺ and FOLR2⁻ macrophages. All donors were nondiseased (n = 6 eyes). Student's t test. **(O)** Flow cytometry MFI of LDLR, SCARB1, MSR1, CD206, and ABCA1 staining in FOLR2⁺ and FOLR2⁻ macrophages. All donors were nondiseased (n = 9 eyes). Student's t test. **(P)** LC/MS lipidomics from FACS-sorted FOLR2⁺ and FOLR2⁻ macrophages from a nondiseased donor. Lipid abundances are shown for FOLR2⁺ macrophages relativized to FOLR2⁻ macrophages. VLC = very long chain; SM = sphingomyelin; LacCer = lactosylceramide; PC= phosphatidylcholine; Cer = ceramide; DG = diglyceride; ST = sterol; MG = monoglyceride; HexCer = hexosylceramide; PC = phosphatidylcholine; TG = triglyceride; PE = phosphatidylethanolamine. **P ≤ 0.01; ***P ≤ 0.001; ****P ≤ 0.0001.

macrophage populations, which appeared to occupy the same general niche (Fig. 2 F). FOLR2⁺ macrophages were large, elongated with pseudopodia, and co-stained with LYVE1, while FOLR2⁻ macrophages were small, round, and co-stained with CD11c (Fig. 2 F).

To better understand the unique gene regulatory networks that govern these two macrophages, we performed a differential gene expression (DGE) analysis comparing the FOLR2⁺ versus FOLR2⁻ populations. In FOLR2⁺ macrophages, 902 genes were upregulated and 3,762 were downregulated (Fig. 2 G). Among the upregulated genes were several involved in phagocytic/lysosomal processes (CD63, CTSB, CTSC, CLTA, GNAS, LGALS1, LGALS3, C1QA, C1QC, and C1QB), antioxidant enzymes (GPX1 and GPX3), and lipid metabolism (phospholipid transfer protein [PLTP], NPC2, APOE, and CD36; Fig. 2 G). Downregulated genes included several cytokines/chemokines (IL1B, CXCL8, CCL3, TNF, CCL4, CXCL3, IL1A, and IL23A), proinflammatory transcription factors (NFKB1, REL, STAT3, RELB, CREB1, STAT1, NFKB2, IRF1, and IRF8), pattern recognition receptors (TLR2, NLRP3, TLR1, and TLR4), hypoxia-associated genes (HIF1A, EPAS1, VEGFA, and PDGFB), and cytokine signaling machinery (JAK1, IL6R, IFNGR1, IRAK3, IRAK2, MAP4K3, NFATC1, NFATC2, TRAF1, JAK2, MAPK14, MAPK1, and TRAF3; Fig. 2 G). Moreover, 19 of 46 (41.3%) known AMD risk genes (Fritsche et al., 2016) were upregulated in FOLR2⁻ macrophages (VEGFA, KMT2E, ABCA1, ARHGAP21, RAD51B, PILRA, SRPK2, CETP, C9, TGFBR1, NPLOC4, MMP9, PILRB, TIMP3, SYN3, ACAD10, CNN2, HTRA1, and TNFRSF10A) versus just 1 (2.2%; CD63) in FOLR2⁺ macrophages (Fig. 2 G). Gene set enrichment analyses (GSEA) of the upregulated genes in FOLR2⁺ macrophages revealed enrichment in oxidative phosphorylation, proteasome degradation, antigen presentation, antioxidant processes, and several pathways involved in lipid metabolism: (1) VLDLR internalization and degradation, (2) fatty acid binding, (3) lipoprotein remodeling and clearance, and (4) PPARα pathway (Fig. 2 H). Conversely, pathways enriched in FOLR2⁻ macrophages included several involved in inflammation: (1) TNFα signaling via NFκB, (2) cellular response to IL-1, (3) inflammatory response, (4) prostaglandin signaling, and (5) cellular response to calcium ion (Fig. 2 H).

A defining feature of AMD is dysfunctional lipid handling in the posterior segment, which classically manifests as the accumulation of drusen deposits within the choroid (Curcio et al., 2011). Therefore, given the preponderance of lipid metabolism pathways upregulated in FOLR2⁺ macrophages, we further investigated this association. In choroidal whole mounts, we stained for neutral lipid droplets using the dye Nile red and for PLTP, an enzyme enriched in FOLR2⁺ macrophages that remodels high-density lipoprotein (HDL) particles (Masson et al., 2009) (Fig. 2 I). PLTP⁺ macrophages colocalized with bright Nile red staining, suggesting a high lipid content in FOLR2⁺ macrophages (Fig. 2 I). To confirm this, we performed flow cytometry on choroidal digests stained with Nile red and compared the amount of lipid contained within the two macrophage populations (Fig. 2 J). Among the nine nondiseased eyes, FOLR2⁺ macrophages had significantly greater lipid content than FOLR2⁻ macrophages (Fig. 2 K). Next, to assess the functional capacity of choroidal macrophages with respect to lipoprotein metabolism, we incubated freshly isolated donor choroids with fluorescently labeled low-density lipoproteins (dil-LDL) and then measured lipoprotein uptake 4 h later. IBA1⁺ choroidal macrophages stained brightly for dil-LDL, confirming that these cells directly uptake lipoprotein particles (Fig. 2 L). We performed flow cytometry on digested choroids that had been previously incubated with dil-LDL and compared the amount of dil-LDL within the two macrophage populations (Fig. 2 M). Relative to FOLR2⁻ macrophages, the FOLR2⁺ group contained significantly greater dil-LDL (Fig. 2 N). We next compared the protein expression of several key lipid metabolism mediators, including LDLR, SCARB1 (SR-B1), MSR1, CD206 (MRC1), and ABCA1, all of which were significantly increased in the FOLR2⁺ macrophages (Fig. 2 O). Lastly, to understand the types of lipids contained within choroidal macrophages, we FACS sorted the FOLR2⁺ and FOLR2⁻ populations and then performed global lipidomics using liquid chromatography–mass spectrometry (LC/MS). The abundances of nearly all detected lipid species, with the exception of phospholipids, were increased in FOLR2⁺ macrophages relative to that of the FOLR2⁻ subset (Fig. 2 P). The lipid species with the greatest fold change were sphingomyelins, especially very long-chain sphingomyelins, followed next by cholesterol esters (Fig. 2 P). These data lead us to conclude that FOLR2⁺ macrophages are a homeostatic subset of phagocytes that are intimately involved in lipid metabolism within the human choroid.

FOLR2⁺ choroidal macrophages are decreased and dysfunctional in AMD

To explore whether FOLR2⁺ choroidal macrophages may be implicated in AMD, we began by investigating the frequency of these cells in healthy and diseased donor choroids. After filtering, the human choroid scRNA-seq dataset contained 28 donors with reported AMD (42.9% early/intermediate AMD, 42.9% atrophic AMD, and 14.3% neovascular AMD) and 28 nondiseased adult donors. Relative to all myeloid cells, FOLR2⁺ macrophages were significantly decreased in the choroids from AMD donors (Fig. 3 A). The macula, where AMD classically manifests, showed the greatest decrease compared with nondiseased donors (62.2 ± 36.1% versus 16.8 ± 33.9%; nondiseased versus AMD, respectively; median ± IQR) (Fig. 3 A). FOLR2⁺ macrophages were also significantly decreased in the peripheral choroid (31.9 ± 34.9% versus 14.0 ± 23.8%) (Fig. 3 A). Conversely, the frequencies of FOLR2⁻ macrophages were not statistically different in either the macula or peripheral choroids of nondiseased versus AMD donors per scRNA-seq (Fig. S4 A). To further strengthen these findings, we used publicly available bulk RNA-sequencing (bulk RNA-seq) data (GSE135092) containing 266 human RPE/choroid samples across 129 donors to infer the frequency of FOLR2⁺ macrophages (Orozco et al., 2020). In agreement, the expression of FOLR2 was significantly decreased compared with nondiseased controls in both the macular and peripheral AMD samples (Fig. 3 B). We next used the scRNA-seq data to identify the genes that are most specific to FOLR2⁺ macrophages compared with all other cells of the choroid, which returned 17 genes (Fig. 3 C). Comparing the expression of these 17 genes across the full bulk RNA-seq cohort revealed a broad reduction in both macular and peripheral AMD samples (Fig. 3 D).

To confirm the decrease of FOLR2⁺ macrophages in AMD, we obtained donor eyes with confirmed AMD, performed flow cytometry on dissociated choroid, and compared frequencies to that of nondiseased donors. To do this, we received 30 whole globes from 15 donors. Ex vivo fundus and optical coherence tomography (OCT) imaging were performed to determine disease status (Fig. 3 E), and ophthalmic records were obtained, when available, to confirm diagnoses. Of these 30 globes, 10 eyes from 5 donors had diabetic retinopathy and were excluded. Nine eyes from five donors (Table S1) showed no indication of drusen or posterior segment disease on ex vivo imaging (grade 1 on Minnesota grading scale; Fig. S2 A) or ophthalmic records (Table S2) and were thus enrolled in the nondiseased cohort. 10 eyes from 5 donors (Table S1) had AMD, including 4 donors with a confirmed ophthalmic history of AMD, 2 of which had been previously treated with anti-VEGF injections (Table S2). On ex vivo imaging, 60% of AMD globes were grade 4 and 40% were grade 3 using the Minnesota grading system (Fig. S2 B). For the nondiseased cohort, the mean age was 70 years, 80% were male, and 40% had a history of diabetes (Table S1). For the AMD cohort, the mean age was 86 years, 40% were male, and 40% had a history of diabetes (Table S1).

Flow cytometry on choroidal digests showed that, in nondiseased eyes, FOLR2⁺ macrophages predominated and FOLR2⁻ macrophages were sparse (Fig. 3 F). Conversely, in AMD donors, FOLR2⁺ macrophages were decreased and the relative proportions of FOLR2⁻ macrophages were increased (Fig. 3 F). Relative to all macrophages, the FOLR2⁺ subset was significantly reduced in the AMD globes (70.4 ± 24.2% versus 50.1 ± 27.6%) (Fig. 3 G). In addition, we measured the absolute count of FOLR2⁺ macrophages per mm² of choroidal tissue, which again showed that the FOLR2⁺ subset was significantly reduced in the AMD cohort (57.0 ± 39.1 versus 22.3 ± 26.4) (Fig. 3 H). For FOLR2⁻ macrophages, their relative frequencies were significantly increased in the AMD cohort, but their absolute counts per mm² were not (Fig. S4 B). Consistent with this observed reduction in FOLR2⁺ macrophages, cleaved caspase 3, a marker of apoptosis, was significantly increased in FOLR2⁺ macrophages from AMD choroids, while Ki67, a marker of proliferation, was decreased (Fig. 3 I). Using immunofluorescence on choroidal whole mounts, we confirmed that the nondiseased choroid contained numerous FOLR2⁺ IBA1⁺ macrophages with strong Ki67 staining, while the AMD choroid did not (Fig. 3 J). Thus, using three independent methods (scRNA-seq, bulk RNA-seq, and flow cytometry), we show that FOLR2⁺ macrophages are decreased in the AMD choroid.

Given the reduced frequency of FOLR2⁺ macrophages in AMD, we next sought to understand the gene expression network in these cells during disease. We performed a DGE analysis comparing macular FOLR2⁺ macrophages in AMD versus nondiseased donors, which returned 796 genes, including 499 upregulated and 297 downregulated (Fig. 3 K). Upregulated genes included those associated with cytokines/chemokines (IL18, CXCL1, and CCL5), NFκB (REL, NFKB1, and TLR2), complement receptors (C3AR1 and C5AR1), hypoxia (HIF1A and LDHA), and lipid synthesis (ACSL1, ACSL3, and HMGCS1; Fig. 3 K). Conversely, downregulated genes included FOLR2 itself as well as several associated with homeostatic lipid clearance (PLTP, NPC2, TREM2, and APOC1) and phagolysosomal processes (CTSZ, CTSL, GNAS, CTSB, HEXB, CTSC, CTSD, and LAMP1; Fig. 3 K). FOLR2⁻ macrophages from AMD donors showed similar upregulation of cytokines, chemokines, and inflammatory mediators (Fig. S4, C and D). GSEA analysis confirmed an enrichment of various homeostatic processes in nondiseased FOLR2⁺ macrophages, including oxidative phosphorylation, clathrin-mediated endocytosis, and plasma lipoprotein clearance (Fig. 3 L). Conversely, pathways enriched in AMD FOLR2⁺ macrophages included positive regulation of cell death, hypoxia, cytokine signaling, and complement receptor activity (Fig. 3 L).

Next, to assess the functional ability of FOLR2⁺ macrophages to clear lipoproteins, we incubated freshly dissected choroids from nondiseased and AMD donors with fluorescently labeled LDL and compared uptake in choroidal macrophages. While nondiseased choroids showed strong uptake of dil-LDL in IBA1⁺ choroidal macrophages, AMD choroids revealed diffuse dil-LDL that lacked the strong punctate staining observed in nondiseased choroidal macrophages (Fig. 3 M). Flow cytometry on digested choroids that had been previously incubated with dil-LDL confirmed significantly decreased dil-LDL uptake by FOLR2⁺ macrophages in AMD choroids (Fig. 3, N and O). Similarly, Nile red staining demonstrated significantly reduced neutral lipid in FOLR2⁺ macrophages from AMD donors (Fig. 3 P). For FOLR2⁻ macrophages, Nile red staining showed no difference in

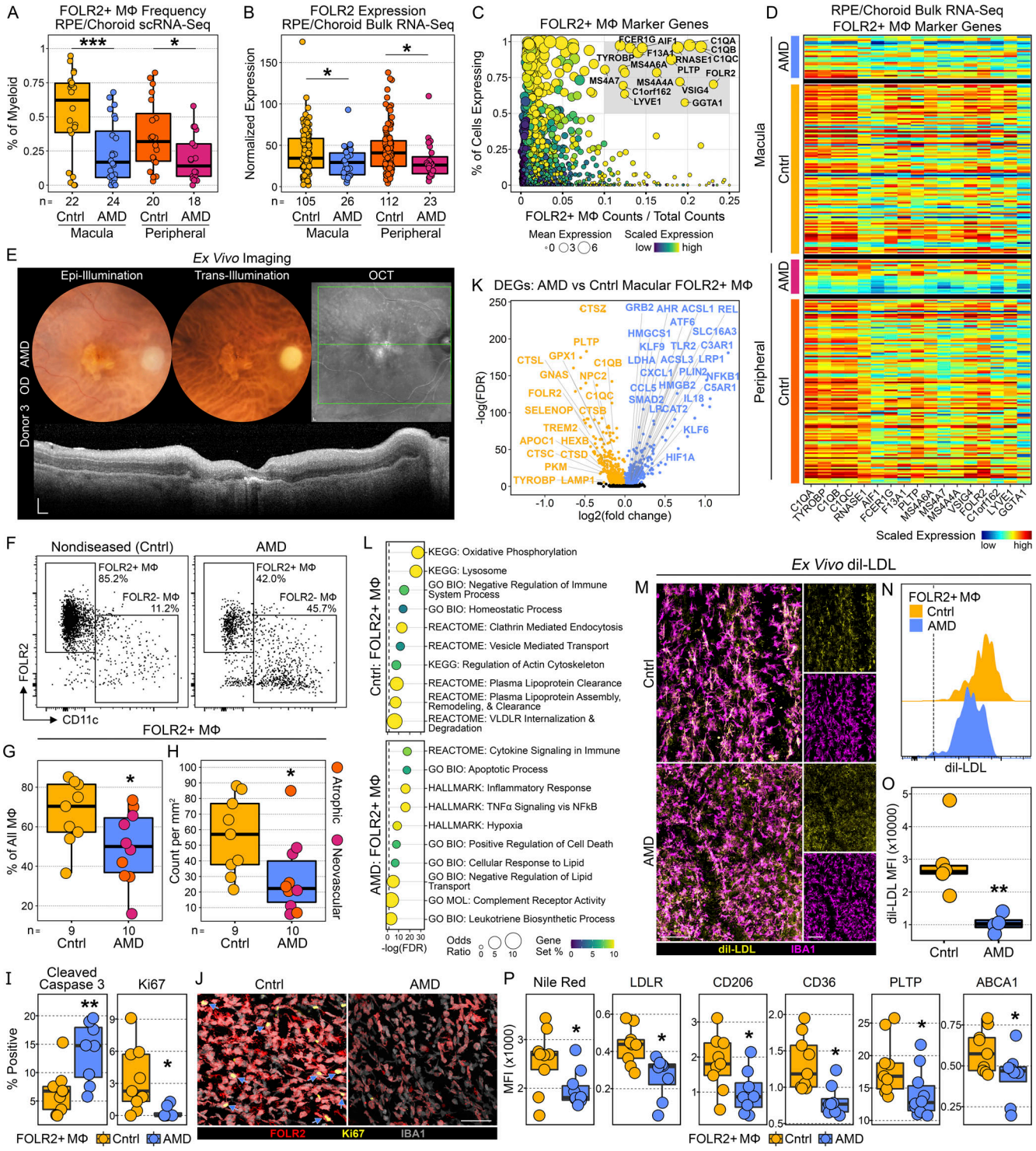

Figure 3. **Decline and dysfunction of FOLR2⁺ choroidal macrophages in AMD. (A)** Frequency of FOLR2⁺ macrophages (MΦ) in scRNA-seq data relative to all myeloid cells. Sample sizes represent unique donors by location and disease group. One-way ANOVA with Holm–Sidak correction. **(B)** FOLR2 normalized gene expression in RPE/choroid bulk RNA-seq data. Sample sizes represent unique donors by location and disease group. One-way ANOVA with Holm–Sidak correction. **(C)** Plot showing marker genes of FOLR2⁺ macrophages from scRNA-seq data. Marker genes highlighted by gray box are those used for the heatmap in D. X axis shows proportion of raw counts derived from FOLR2⁺ macrophages divided by the total raw counts for that gene. **(D)** Heatmap of the top 17 marker genes for FOLR2⁺ macrophages from C. **(E)** Example of ex vivo imaging from an AMD donor eye. Top left = fundus image using epi-illumination. Top middle = fundus image using trans-illumination. Top right = en-face OCT showing location of B scan below. Scale bars = 200 µm. **(F)** Representative flow cytometry plots from nondiseased (left) and AMD (right) donors showing FOLR2⁺ and FOLR2⁻ macrophages. **(G)** Frequency of FOLR2⁺ macrophages relative to all macrophages from flow cytometry. Sample sizes are individual eyes. Atrophic AMD (orange) and neovascular AMD (magenta). Student's *t* test. **(H)** Absolute counts of FOLR2⁺ macrophages per mm² of choroidal tissue from flow cytometry. Sample sizes are individual eyes. Atrophic AMD (orange) and neovascular AMD (magenta). Student's *t* test. **(I)** Flow cytometry percent positive staining for cleaved caspase 3 and Ki67 staining in FOLR2⁺ macrophages from nondiseased (*n* =

9 eyes) and AMD (n = 8) donors. Student's t test. **(J)** Representative immunofluorescence of nondiseased and AMD choroids stained with FOLR2, Ki67, and IBA1. Scale bar = 100 µm. **(K)** Volcano plot of differentially expressed genes (DEGs) in AMD versus nondiseased macular FOLR2$^+$ macrophages from scRNA-seq data. Blue = genes upregulated in AMD (499 genes). Yellow = genes upregulated in nondiseased (297 genes). **(L)** GSEA of DEGs from K showing selected pathways. Dashed lines represent significance cutoffs. **(M)** Representative immunofluorescence of human choroids incubated with dil-LDL from nondiseased (top) and AMD (bottom) donors. Scale bars = 100 µm. **(N)** Histograms of dil-LDL staining in FOLR2$^+$ macrophages from representative nondiseased and AMD donors. Dashed line is cutoff from negative control. **(O)** Flow cytometry MFI of dil-LDL staining in FOLR2$^+$ macrophages from nondiseased (n = 6 eyes) and AMD (n = 4 eyes) choroids. Student's t test. **(P)** Flow cytometry MFI of Nile red, LDLR, CD206, CD36, PLTP, and ABCA1 staining in FOLR2$^+$ macrophages from nondiseased (n = 9 eyes) and AMD (n = 8 eyes) donors. Student's t test. *P ≤ 0.05; **P ≤ 0.01; ***P ≤ 0.001. MFI; mean fluorescent intensity.

nondiseased versus AMD choroids, whereas dil-LDL uptake was significantly reduced in AMD samples (Fig. S4, E and F). Lastly, we compared the protein expression of several key mediators of lipoprotein clearance in FOLR2$^+$ macrophages. FOLR2$^+$ macrophages from AMD donors displayed significant reductions in the canonical LDL receptor LDLR, the scavenger receptor CD36, the mannose receptor CD206, the HDL remodeler PLTP, and the reverse cholesterol transporter ABCA1 (Fig. 3 P). Together these findings establish that AMD is associated with dysfunctional lipid handling in choroidal macrophages.

Temporal dynamics and ontogeny of murine FOLR2$^+$ choroidal macrophages

To investigate FOLR2$^+$ choroidal macrophages in further detail, we next studied this population in mice. Flow cytometry on mouse choroidal digests (Fig. S3 D) revealed that, unlike humans where FOLR2$^+$ macrophages represent the majority of choroidal phagocytes, in mice, this population transitions to the minority fraction by early adulthood (Fig. 4 A). Murine FOLR2$^+$ macrophages were highest in early development and then decreased precipitously, reaching a steady state by 3 mo of age (Fig. 4, A and B). During this sharp decline, FOLR2$^+$ macrophages gained MHCII expression, suggestive of a change in phenotype (Fig. 4, A and C). In adult mice, the predominant choroidal macrophage population is MHCII$^+$ FOLR2$^-$, which accounts for roughly 60% of all choroidal macrophages (Fig. 4, A and D). At postnatal day 14 (P14), this population appeared in equivalent frequency to that of the MHCII$^-$ FOLR2$^+$ macrophages (Fig. 4, A and D). Yet, by P28, MHCII$^+$ FOLR2$^-$ macrophages more than doubled in frequency, while MHCII$^-$ FOLR2$^+$ macrophages were halved (Fig. 4, A and D). Despite these key differences between murine and human choroidal phagocytes, roughly 10% of adult murine macrophages maintained FOLR2 expression out to 2 years of age (Fig. 4, A and D).

The most recent study on the ontogeny of murine choroidal macrophages, using Cx3cr1-CreERT2 mice, suggested that these cells might be short lived and adult derived (O'Koren et al., 2019). However, others have shown that IBA1$^+$ MPs populate the mouse choroid during early embryonic development (McMenamin et al., 2020; Santos et al., 2008), and our results on early temporal dynamics of FOLR2$^+$ choroidal macrophages hint that this population may be prenatally derived. Therefore, to address this question, we used the *Ms4a3* fate reporter, which is the current state-of-the-art monocyte-derived transgenic mouse model (Liu et al., 2019). *Ms4a3* is a gene that is highly specific to granulocyte-monocyte progenitors, and its expression is entirely absent in prenatal hematopoiesis. Therefore, macrophages that lack the *Ms4a3* fate reporter are prenatally derived. In the P14 eye, a large population of IBA1$^+$ macrophages was negative for the MS4A3-TdTomato fate reporter (Fig. 4 E). These MS4A3$^-$ macrophages were evenly distributed and lacked any obvious morphological distinctions compared with their MS4A3$^+$ postnatally derived counterparts (Fig. 4 E). Over normal aging, MS4A3$^+$ choroidal macrophages gradually increased in frequency, consistent with replacement of prenatally derived macrophages through definitive hematopoiesis (Fig. 4, F and G). However, this increase in MS4A3$^+$ macrophages was entirely restricted to the FOLR2$^-$ population (Fig. 4, F and H). By 6 mo of age, the proportion of MS4A3$^+$ cells in the FOLR2$^+$ population remained stable at ∼10% (Fig. 4, F and H), suggesting that FOLR2$^+$ choroidal macrophages are prenatally derived and self-maintained with minimum input from definitive hematopoiesis.

Chronic depletion of FOLR2$^+$ choroidal macrophages in healthy mice elicits an accelerated, AMD-like phenotype

We next sought to understand the functional consequences of depleting the FOLR2$^+$ pool of choroidal macrophages in healthy adult mice. To this end, we utilized the LYVE1^{Cre} transgenic mouse, since both human and mouse FOLR2$^+$ choroidal macrophages specifically co-express LYVE1 (Fig. 5 A). We crossed LYVE1^{Cre} mice with CSF 1 receptor (CSF1R)$^{LoxP\text{-}stop\text{-}LoxP\text{-}DTR}$ mice, which produce diphtheria toxin receptor (DTR) in CSF1R-expressing cells upon Cre-recombinase cleavage. Thus, this model allows diphtheria-mediated ablation of FOLR2$^+$/LYVE1$^+$ macrophages. To facilitate chronic choroidal macrophage depletion, we developed a method to deliver diphtheria toxin via topical eye drops (Fig. 5 B). After 3 days of topical diphtheria toxin, a dose-dependent loss of FOLR2$^+$ choroidal macrophages was observed, confirming our experimental approach (Fig. 5 C). Using this topical diphtheria model, we administered daily eye drops for 3 wk to investigate the effect of chronic FOLR2$^+$ macrophage depletion on choroidal and visual health (Fig. 5 B). Flow cytometry after 3 wk of daily topical diphtheria demonstrated specific depletion of the MHCII$^+$ FOLR2$^+$ choroidal macrophages (Fig. 5, D and E). Importantly, MHCII$^+$ FOLR2$^-$ macrophages were unchanged (Fig. 5, D and E), as were the frequencies of monocytes and neutrophils (Fig. 5 F). Total macrophages showed a partial depletion as expected (Fig. 5 F). In CSF1R^{DTR} mice that lacked the LYVE1^{Cre} transgene, diphtheria toxin had no effect on choroidal macrophage frequencies (Fig. S5 A) and did not cause ocular toxicity (Fig. S5 B).

After 1 wk of daily topical diphtheria-mediated depletion of FOLR2$^+$ choroidal macrophages, we observed thinning of the choroidal layer on OCT imaging (Fig. 5 G), which was significant compared with mice treated with vehicle (Fig. 5 H). Fundus imaging in these mice revealed mild pigmentary changes and

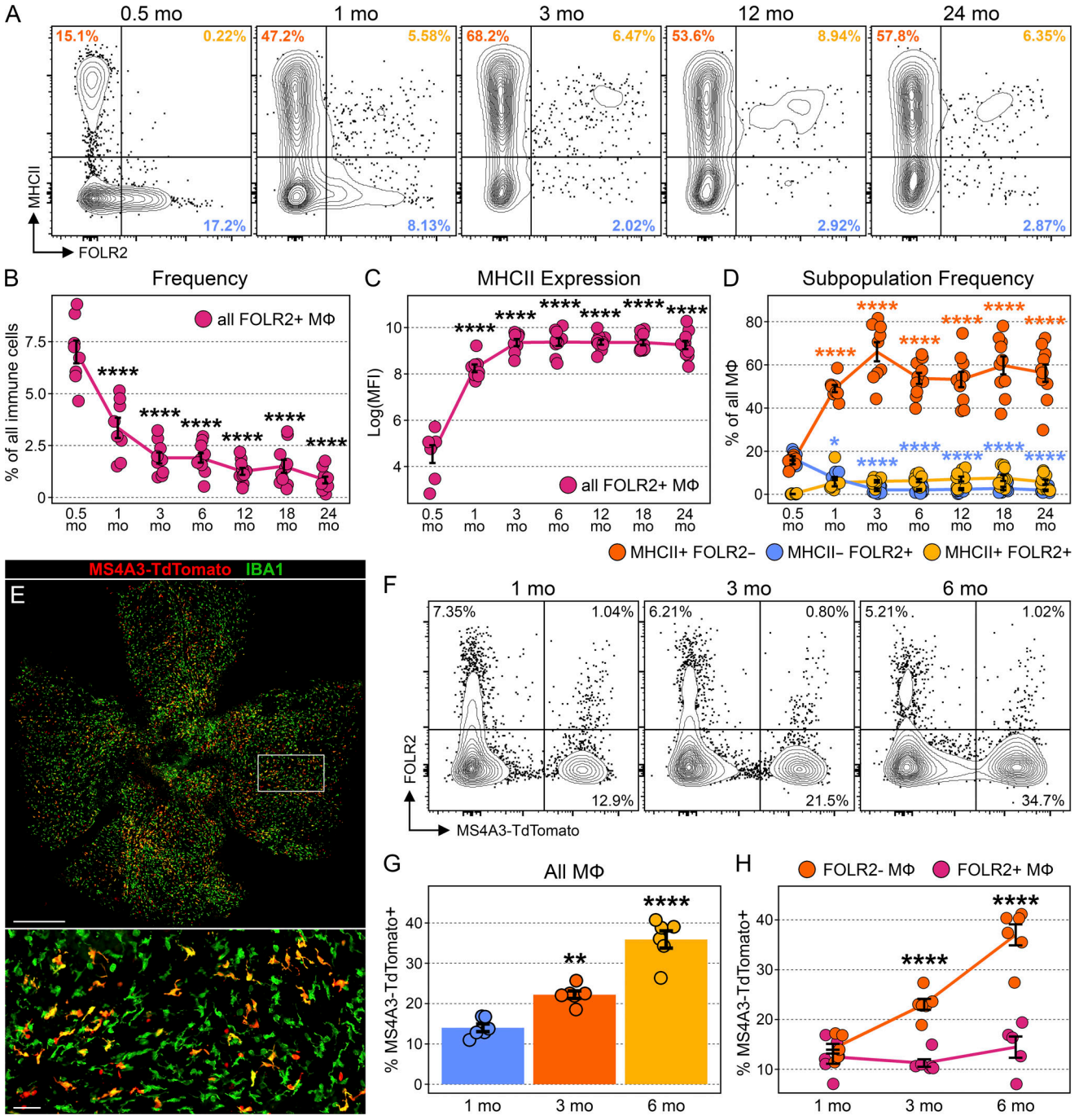

Figure 4. **Temporal dynamics and ontogeny of murine FOLR2⁺ choroidal macrophages. (A)** Representative flow cytometry plots of choroidal macrophages from different aged wild-type mice. **(B)** Flow cytometry frequencies of FOLR2⁺ choroidal macrophages relative to all immune cells across different aged wild-type mice. *n* = 8 eyes for 0.5 and 1 mo; *n* = 9 eyes for 3 mo; *n* = 10 eyes for 6, 12, 18, and 24 mo. One-way ANOVA with Holm correction. Statistical comparisons were made to the 0.5-mo time point. **(C)** Log transformed MFI of MHCII expression in FOLR2⁺ macrophages from flow cytometry across different aged wild-type mice. *n* = 8 eyes for 0.5 and 1 mo; *n* = 9 eyes for 3 mo; *n* = 10 eyes for 6, 12, 18, and 24 mo. One-way ANOVA with Holm correction. Statistical comparisons were made to the 0.5-mo time point. **(D)** Flow cytometry frequencies of MHCII⁺FOLR2⁻, MHCII⁺FOLR2⁺, and MHCII⁻FOLR2⁺ choroidal macrophages relative to all macrophages across different aged wild-type mice. *n* = 8 eyes for 0.5 and 1 mo; *n* = 9 eyes for 3 mo; *n* = 10 eyes for 6, 12, 18, and 24 mo. Two-way ANOVA with Holm correction. Intragroup statistical comparisons were made to the 0.5-mo time point. **(E)** Whole mount immunofluorescence of choroid/sclera from 0.5 mo MS4A3^{TdTomato} fate-reporter mouse. Top image scale bar = 500 µm. Bottom image scale bar = 50 µm. **(F)** Concatenated flow cytometry of mouse choroids from 1, 3, and 6 mo MS4A3^{TdTomato} fate-reporter mice. **(G)** Frequencies of total MS4A3^{TdTomato}-positive choroidal macrophages (MΦ) relative to all macrophages. *n* = 6 eyes per time point. One-way ANOVA with Holm correction. Statistical comparisons were made to the 1-mo time point. **(H)** Frequencies of MS4A3^{TdTomato}-positive choroidal macrophages in FOLR2⁺ and FOLR2⁻ macrophage populations. *n* = 6 eyes per time point. Two-way ANOVA with Holm–Sidak correction. Intragroup statistical comparisons were made to the 1-mo time point. *P ≤ 0.05; **P ≤ 0.01; ****P ≤ 0.0001. MFI; mean fluorescent intensity.

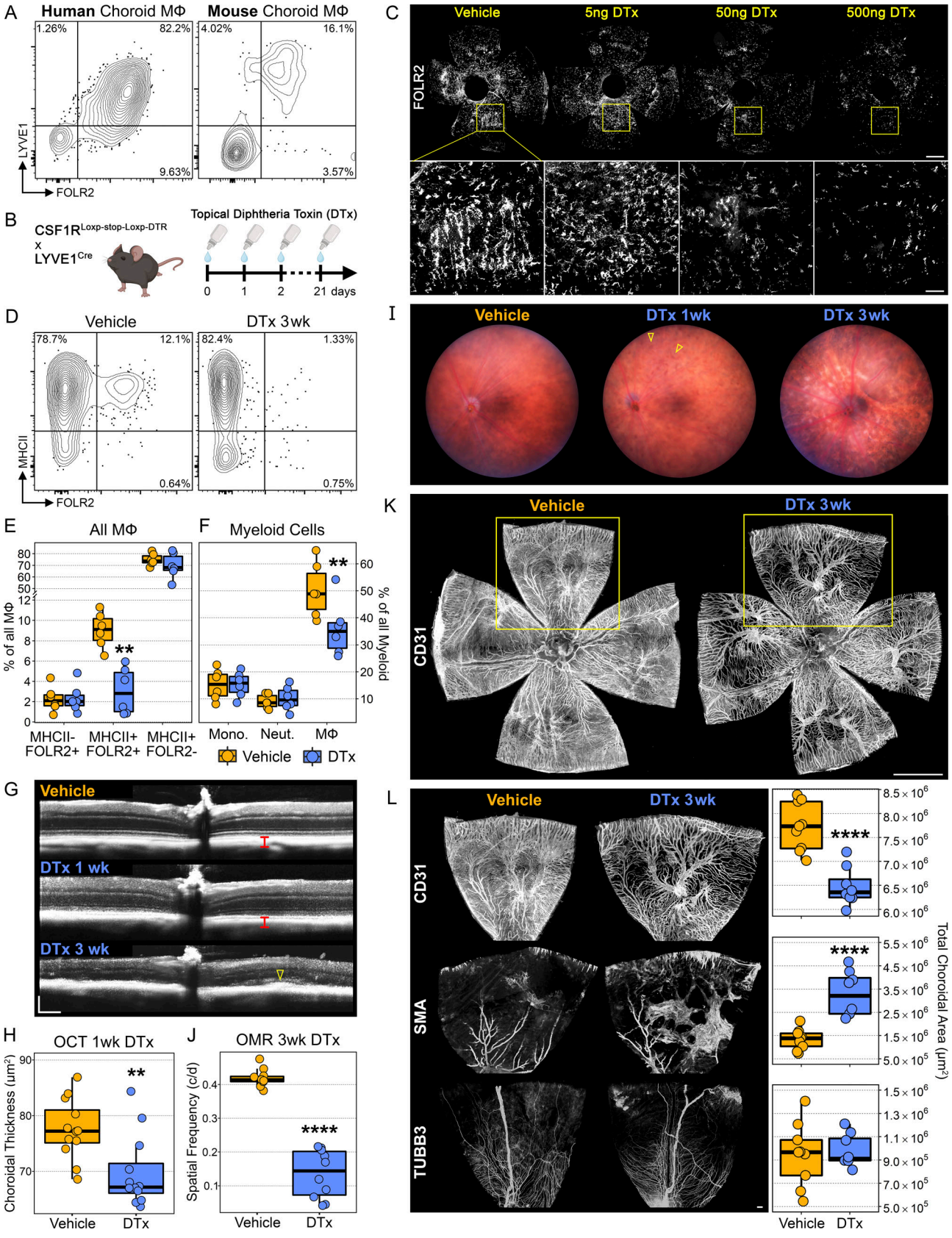

Figure 5. **Chronic depletion of FOLR2⁺ choroidal macrophages causes overt posterior segment pathology. (A)** Representative flow cytometry of macrophages (MΦ) from human (left) and mouse (right) choroids showing LYVE1 and FOLR2 co-expression. **(B)** Graphic showing transgenic mouse line used for diphtheria depletion of FOLR2⁺ macrophages and timeline of daily topical diphtheria administration for 3 wk of chronic depletion. **(C)** Whole mount

immunofluorescence of FOLR2 staining in mouse choroid/sclera from LYVE1^{Cre}/CSF1R^{DTR} mice treated for 3 consecutive days with either vehicle or escalating doses of diphtheria toxin (DTx; 5, 50, 500 ng). Yellow boxes indicate locations of magnified fields of view (lower row) for each respective experimental group. Top scale bar = 500 µm. Bottom scale bar = 100 µm. **(D)** Representative flow cytometry showing choroidal macrophages from vehicle and 3 wk topical DTx mice. **(E)** Choroidal macrophage quantifications from flow cytometry of vehicle and 3 wk topical DTx mice. Frequencies are relative to all macrophages. Yellow = vehicle. Blue = DTx. *n* = 6 eyes per group. Two-way ANOVA with Holm–Sidak correction. **(F)** Myeloid quantifications from flow cytometry of vehicle and 3 wk topical DTx mice. Frequencies are relative to all myeloid cells. Mono. = monocytes; Neut. = neutrophils; MΦ = choroidal macrophages. Yellow = vehicle. Blue = DTx. *n* = 6 eyes per group. Two-way ANOVA with Holm–Sidak correction. **(G)** Representative OCT of LYVE1^{Cre}/CSF1R^{DTR} mice treated with vehicle, 1 wk of topical DTx, or 3 wk topical DTx. Red "I" shows choroidal thickness in vehicle group and is same size in both images. Yellow arrowhead shows area of hyperreflective protrusion. Scale bar = 100 µm. **(H)** Quantification of choroidal thickness from OCT images in G. *n* = 12 eyes per group. Student's *t* test. **(I)** Representative fundus images from vehicle, 1 wk topical DTx, and 3 wk topical DTx. Yellow arrowhead shows area of pigment clumping. **(J)** Quantification of optomotor response (OMR) test from vehicle versus 3 wk topical DTx. *n* = 10 eyes per group. Student's *t* test. **(K)** Representative CD31 whole mount immunofluorescence of choroid/sclera from vehicle and 3 wk topical DTx mice. Yellow boxes indicate whole mount quadrant shown for CD31 in panel L. Scale bar = 1 mm. **(L)** Representative whole mount immunofluorescence of choroid/sclera from vehicle (*n* = 9 eyes) and 3 wk topical DTx mice (*n* = 8 eyes). Note that whole mount quadrants are shown, but the entire choroid was used in quantifications. Quantifications of the total area of staining (µm^2) are shown on right. Same anatomical location shown in quadrant images. CD31 = vasculature, SMA = fibrosis, and TUBB3 = innervation. Scale bar = 100 µm. Student's *t* test. **P ≤ 0.01; ****P ≤ 0.0001.

occasional RPE clumping (Fig. 5 I). However, in this same cohort of mice, after 3 wk of daily topical depletion of FOLR2$^+$ choroidal macrophages, gross pathology of the posterior segment was evident. This included retinal thinning with hyperreflective subretinal material on OCT (Fig. 5 G) and large pigmentary changes with retinal lesions on fundus imaging (Fig. 5 I). Consistent with this observed pathology, visual acuity in these mice using the optomotor response test revealed attenuated vision compared with the vehicle-treated cohort (Fig. 5 J). We performed immunofluorescence on choroidal whole mounts to assess changes in vascular coverage, fibrosis, and choroidal innervation after chronic depletion of FOLR2$^+$ choroidal macrophages (Fig. 5, K and L). After 3 wk of daily topical diphtheria treatment, we observed dramatic vasodegeneration of the choriocapillaris (Fig. 5, K and L), a hallmark finding in human AMD eyes (McLeod et al., 2009; Mullins et al., 2011). SMA staining revealed patches of severe fibrosis (Fig. 5 L), which corresponded to the hyperreflective subretinal material observed on OCT imaging (Fig. 5 G). Despite these dramatic structural changes, FOLR2$^+$ macrophage depletion had no effect on choroidal nerve density (Fig. 5 L). These data demonstrate that FOLR2$^+$ macrophages are required for the homeostatic maintenance of the choroid and that the loss of these cells in otherwise healthy mice results in an accelerated AMD-like phenotype.

Depletion of FOLR2$^+$ macrophages in the disease setting worsens CNV

Lastly, we sought to understand the effect of depleting FOLR2$^+$ choroidal macrophages in the disease setting. To this end, we utilized the laser-induced CNV model, which is the most widely studied murine model of AMD (Pennesi et al., 2012). We pretreated LYVE1^{Cre}/CSF1R$^{LoxP\text{-}stop\text{-}LoxP\text{-}DTR}$ mice for 7 days with either vehicle or topical diphtheria toxin, performed laser-induced rupture of Bruch's membrane, and then continued topical diphtheria treatment for 7 more days until our experimental endpoint. 7 days after laser induction, CNV lesion size was significantly increased in the FOLR2$^+$ macrophage depletion group (Fig. 6, A and B). Using flow cytometry on choroidal digests, we found that monocyte and neutrophil recruitment were increased and that total macrophages were decreased in the diphtheria treatment group (Fig. 6, C and D). Within the choroidal macrophage pool, both MHCII$^+$ FOLR2$^+$ and MHCII$^-$ FOLR2$^+$ macrophages were decreased compared with vehicle-treated laser CNV (Fig. 6, E and F). Surprisingly, MHCII$^+$ FOLR2$^-$ macrophages were significantly increased in the diphtheria depletion group (Fig. 6, E and F), a finding that was not observed when FOLR2$^+$ choroidal macrophages were decreased at baseline in healthy mice (Fig. 5, D and E). Interestingly, this increase in MHCII$^+$ FOLR2$^-$ cells was entirely due to an expansion of CD11c$^+$ macrophages (Fig. 6, G and H). This result suggests that, in the disease setting, loss of FOLR2$^+$ choroidal macrophages either induces the recruitment of CD11c$^+$ phagocytes and/or promotes the differentiation of extravasated monocytes to this subset.

Prior work has established that CD11c$^+$ macrophages are proangiogenic in laser-induced CNV (Droho et al., 2023) and that macrophages are enriched on human CNV lesions in AMD (Lopez et al., 1993; Sarks et al., 1997). To investigate the identity of these neovascular-enriched choroidal macrophages and whether these cells contribute to the growth of neovessels, we used 3D multiplex immunofluorescence on human choroid. In a donor with confirmed AMD, we observed an early neovascular lesion, which showed vascular sprouting that stained brightly for UEA-lectin (Fig. 6 I). The lesion was surrounded by strong VEGF staining and was accompanied by fibrotic expansion of perivascular SMA$^+$ mesenchymal cells (Fig. 6 I). VEGF is central to the development of CNV (Campochiaro, 2015), and its neutralization, through the use of intraocular anti-VEGF agents, is the current standard of care in patients with neovascular AMD (Brown et al., 2006; Rosenfeld et al., 2006). In the observed neovascular sprout, VEGF staining overlapped with SMA$^+$ cells as well as with perivascular cells surrounding the lesion, the latter of which co-stained with IL1β (Fig. 6 I). Overlaying LYVE1 and CD11c staining showed that, while LYVE1$^+$ macrophages were largely restricted to the adjacent healthy tissue, CD11c$^+$ macrophages were specifically enriched within the neovascular lesion and closely overlapped with VEGF and IL1β (Fig. 6 I). 3D rendering of the CNV lesion confirmed that the perivascular VEGF and IL1β staining colocalized within the CD11c$^+$ macrophages (Fig. 6 J). These findings reveal that neovascular-enriched choroidal macrophages belong to the CD11c$^+$ FOLR2$^-$ subset and that these cells directly contribute to the growth of

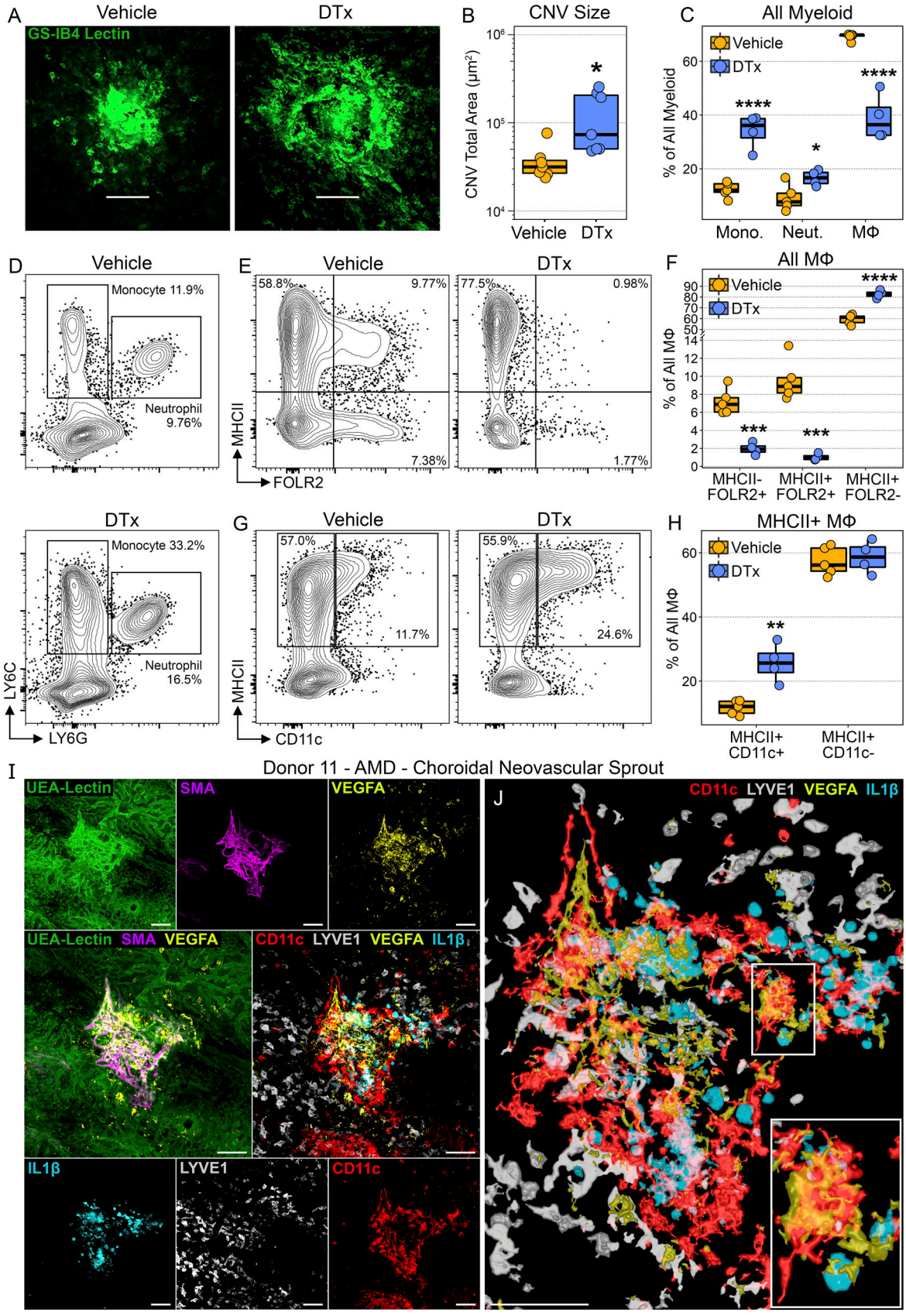

Figure 6. **Targeted elimination of FOLR2⁺ macrophages augments CNV. (A)** Representative laser CNV lesions in vehicle and topical diphtheria toxin (DTx) mice 7 days after laser. GS-IB4 lectin stain (vasculature). Scale bar = 100 µm. **(B)** Quantification of laser CNV lesion size per eye. Areas were averaged over four lesions. *n* = 7 eyes per group. Student's *t* test. **(C)** Myeloid quantifications from flow cytometry of vehicle and DTx CNV mice. Frequencies are relative to all

myeloid cells. Mono. = monocytes; Neut. = neutrophils; MΦ = choroidal macrophages. Yellow = vehicle. Blue = DTx. *n* = 5 eyes for vehicle and *n* = 4 eyes for DTx. Two-way ANOVA with Holm–Sidak correction. **(D)** Representative flow cytometry of all myeloid cells from vehicle and DTx CNV mice showing monocyte and neutrophil gates. **(E)** Representative flow cytometry showing MHCII and FOLR2 staining in choroidal macrophages from vehicle and DTx CNV mice. **(F)** Choroidal macrophage quantifications from flow cytometry of vehicle and DTx CNV mice. Frequencies are relative to all macrophages. Yellow = vehicle. Blue = DTx. *n* = 5 eyes for vehicle and *n* = 4 eyes for DTx. Two-way ANOVA with Holm–Sidak correction. **(G)** Representative flow cytometry showing MHCII and CD11c staining in choroidal macrophages from vehicle and DTx CNV mice. **(H)** MHCII$^+$CD11c$^+$ and MHCII$^+$CD11c$^-$ quantifications from flow cytometry of vehicle and DTx CNV mice. Frequencies are relative to all macrophages. Yellow = vehicle. Blue = DTx. *n* = 5 eyes for vehicle and *n* = 4 eyes for DTx. Two-way ANOVA with Holm–Sidak correction. Vehicle and DTx-treated mice from C–H are the same cohorts shown in Fig. S5 A, along with an additional control cohort treated with DTx under the same experimental conditions. **(I)** Multiplex immunofluorescence of CNV sprout from AMD donor. Maximum intensity projections are shown. Scale bars = 100 µm. **(J)** 3D rendering of neovascular sprout from I. Scale bar = 100 µm. *P ≤ 0.05; **P ≤ 0.01; ***P ≤ 0.001; ****P ≤ 0.0001.

neovessels through paracrine secretion of cytokines and growth factors.

Discussion

Our data establish that prenatally derived FOLR2$^+$ macrophages are essential for choroidal homeostasis and are decreased and dysfunctional in AMD. In humans, we reveal that these cells are intimately involved in choroidal lipid metabolism, a process widely understood to be aberrant in AMD (Curcio et al., 2011). FOLR2$^+$ choroidal macrophages contain high amounts of neutral lipid, directly uptake LDL, and express proteins involved in the remodeling and clearance of lipoprotein particles, all of which are attenuated in AMD. Using three independent methods across 195 total donors, we demonstrate that FOLR2$^+$ choroidal macrophages are decreased in AMD. In murine studies, we use the *Ms4a3* fate reporter to show that FOLR2$^+$ choroidal macrophages are prenatally derived and self-maintained. Chronic depletion of these cells in otherwise healthy mice resulted in an accelerated AMD-like phenotype with severe vasodegeneration of the choriocapillaris, while depletion in the disease setting using the laser-induced CNV model promoted the recruitment of proinflammatory cells and worsened neovascularization. In addition, we provide the first 3D reconstruction of all major cell types in the human choroid and the first complete description of the choroidal immune landscape in humans.

While the majority of our current knowledge on choroidal macrophages is derived from murine studies, it was unclear to what degree the choroidal immune system of the rodent reflected that of our own (McMenamin et al., 2019). Importantly, our data demonstrate significant differences in the immune landscapes of the mouse and human choroids. In humans, we reveal that immune cells are the largest cell population, accounting for nearly half of all nucleated cells in the nondiseased setting, while in mice, immune cells represent <10% of the total choroid. Moreover, in humans, FOLR2$^+$ macrophages account for the majority of MPs (~70%), while in adult mice, the equivalent population is around 10% of the total macrophage pool. These key differences should be considered when interpreting prior work and when designing future studies that aim to extrapolate between mice and humans.

A unifying feature across the various stages and subtypes of AMD is drusen and thus, the loss of lipid homeostasis in the RPE/choroid (Curcio et al., 2011). Normal functioning of the posterior segment requires constant cycling of lipid between the choroid, RPE, and photoreceptors (Lewandowski et al., 2022). Prior work has shown that the RPE packages retina-derived lipidic waste in a type of lipoprotein particle that is secreted basally for removal by the choroidal vasculature (Li et al., 2005a, 2005b; Wang et al., 2009). In AMD, these lipoproteins accumulate in the space directly beneath the RPE basement membrane, suggesting dysfunction in choroidal clearance (Curcio et al., 2011). Whether basally secreted lipoproteins undergo local remodeling by other cell types prior to passive/active diffusion into the choriocapillaris and how lipids are transferred from RPE-derived lipoprotein particles to HDL for systemic removal remain open questions. The tissue-resident choroidal macrophages described in our study directly interact with lipoprotein particles and express a variety of key lipoprotein-specific machinery, including among others, high levels of PLTP, which catalyzes the transfer of phospholipids from triglyceride-rich lipoproteins to HDL, thereby increasing levels of local HDL (Masson et al., 2009). In AMD, PLTP was the third most downregulated transcript in FOLR2$^+$ macrophages, and its protein levels were significantly decreased compared with nondiseased controls.

Our results regarding the role of choroidal macrophages in vascular maintenance and CNV complement and extend prior work. Yang et al. (2020) used a small molecule antagonist of CSF1R and showed that global depletion of macrophages induced vasodegeneration of the choriocapillaris despite no effect on the retinal vasculature (Yang et al., 2020). While these findings were suggestive of a role for choroidal macrophages in vascular maintenance, the results could not be dissociated from the systemic effects of global macrophage depletion. In this work, we pinpoint the causative subpopulation of choroidal macrophages whose depletion, using a novel approach to locally and noninvasively administer diphtheria toxin, resulted in similar pathology. Moreover, the elegant work of Droho et al. (2023) demonstrated that depletion of CD11c$^+$ macrophages attenuated experimentally induced CNV (Droho et al., 2023). These findings are consistent with our own, as targeted elimination of FOLR2$^+$ macrophages induced the recruitment of CD11c$^+$ macrophages in laser CNV, leading to increased lesion size. We confirmed the proangiogenic nature of CD11c$^+$ macrophages in humans using 3D multiplex immunofluorescence of a choroidal neovascular lesion from an AMD choroid, which demonstrated dense perivascular recruitment of CD11c$^+$ macrophages that contained high levels of VEGF and IL1β. Of note, the FOLR2$^+$ choroidal macrophages studied herein appear distinct from the recently described TREM2$^+$ LGALS3$^+$ subretinal microglia attached to the apical RPE in the outer retinas of AMD donor eyes (Yu et al., 2024).

While this work advances our understanding of the immune landscape of the human choroid in health and AMD, many important questions remain. Chief of these is the mechanism responsible for the reduction of FOLR2$^+$ choroidal macrophages in AMD. Our data show that these cells contain elevated levels of cleaved caspase 3 and decreased Ki67, consistent with apoptosis and attenuated proliferation, respectively. Possible causes of this observed phenotype include senescence, inflammatory polarization, susceptibility to a chronic stressor like hypoxia or oxidative stress, or the loss of a survival signal, such as ligands of CSF1R signaling (IL34 and mCSF1). Further experiments are needed. Other notable open questions include the role of the adaptive immune system, especially T cells, in choroidal health and AMD. Despite the eye being the prototypical immune privileged tissue (Niederkorn and Stein-Streilein, 2010), our work confirms that the choroid contains an abundance of innate and adaptive immune cells, which is supported by the relatively high rates of choroiditis and choroidal granulomas observed in patients on immune checkpoint inhibitors (Anquetil et al., 2020; Thibault et al., 2024). While the physiologic role of choroidal T cells is unknown, these cells may be related to the nearby mucous membrane of the conjunctiva (de Paiva et al., 2022), tolerance to retinal antigens (Caspi, 2006), or immune surveillance, especially of the high-density choroidal melanocytes, which have malignant potential (Damato et al., 2011). In breast cancer, FOLR2$^+$ macrophages were positively associated with survival due to their ability to cross-present to CD8 T cells (Ramos et al., 2022), and we observed choroidal macrophages making numerous physical contacts with lymphocytes. 40 years ago, Sarks and colleagues observed choroidal macrophages phagocytosing drusen while simultaneously making physical contact with lymphocytes, suggestive of antigen presentation (Penfold et al., 1984). Whether choroidal T cells play a role in the inflammatory response in AMD remains to be seen. Regardless, understanding these cells is essential to fully appreciating the local choroidal immune system.

FOLR2 is a glycosylphosphatidylinositol-anchored surface receptor that binds to folate and facilitates its internalization through receptor-mediated endocytosis (Nawaz and Kipreos, 2022; Zhao et al., 2011). Folates play an essential role in one-carbon metabolism and are required for a variety of cellular processes, including nucleotide synthesis, methylation, and the interconversion of glycine and serine (Zheng and Cantley, 2019). FOLR2 expression on macrophages was originally described by Nakashima-Matsushita et al. in 1999 in synovial MPs from patients with rheumatoid arthritis (Nakashima-Matsushita et al., 1999). Later research showed that FOLR2 was a specific marker of tumor-associated macrophages in a wide variety of primary tumors (Puig-Kröger et al., 2009). More recent work has demonstrated that most FOLR2$^+$ LYVE1$^+$ macrophages are prenatally derived and self-maintained across multiple different mouse tissues (Dick et al., 2022; Sharma et al., 2020). Although tissue-resident macrophages are known to contain elevated levels of folate, the precise functions of folate and FOLR2 in homeostatic versus inflammatory macrophages remains to be elucidated (Samaniego et al., 2014).

In summary, we show in humans and mice that FOLR2$^+$ choroidal macrophages are a homeostatic, tissue-resident subset that are required for normal functioning of the choroid and are decreased and dysfunctional in AMD. Despite the relatively low frequency of murine FOLR2$^+$ choroidal macrophages, targeted depletion in otherwise healthy mice resulted in severe ocular pathology that shared hallmark features with AMD. Given the essential homeostatic functions of FOLR2$^+$ choroidal macrophages, targeted rejuvenation of this population may represent a novel and cell intrinsic approach to clinical benefit in AMD.

Materials and methods

Mice

All mice were housed at the University of Alabama at Birmingham (UAB). Mice were provided with food and water ad libitum and housed under a 12-h light-dark cycle. All experimental procedures were approved by the UAB Institutional Animal Care and Use Committee. All mice, including transgenic lines and wild type (C57BL/6J), were purchased from Jackson Laboratory and then bred in-house. MS4A3^{Cre} mice (strain no. 036382) were crossed with Ai9 mice (Rosa-CAG-LSL-tdTomato-WPRE; strain no. 007909) to create postnatal hematopoiesis reporters. LYVE1^{Cre} mice (strain no. 012601) were crossed with CSF1R$^{LoxP\text{-}stop\text{-}LoxP\text{-}DTR}$ mice (strain no. 024046) to generate the LYVE1$^+$ macrophage depletion strain.

Human tissue

Whole eye globes from deceased donors were obtained from either Advancing Sight Network (donors 2, 3, 4, 6, 7, 9, 11, and 12) or Eversight. Human donor eyes were procured in accordance with the guidelines of the Declaration of Helsinki, and the use of cadaveric eyes for research was approved by the Institutional Review Board at UAB. Characteristics of each donor are provided in Table S1.

Human choroid dissection, phenotyping, and digestion

Upon receipt of a donor globe, a mark was made at the attachment site of the superior rectus, the anterior chamber was removed, the vitreous was gently decanted, and posterior segments were then submerged in ice-cold oxygenated Ames' buffer (A1420; Millipore Sigma). Ex vivo fundus and OCT (Heidelberg Engineering) imaging (Fig. S2) were performed as previously described (Messinger et al., 2023), and the Minnesota grading system was used for classifying AMD severity (Olsen and Feng, 2004). Imaging findings per eye are presented in Table S2. Globes were then dissected under magnification in a cell culture hood with frequent exchange of ice-cold oxygenated Ames' buffer. A 10-mm diameter corneal trephine was used to collect punch biopsies of the macular RPE/choroid as well as at several sites in the periphery. Larger tissue samples were also isolated using microdissection.

For tissue samples destined for imaging, the RPE was removed with gentle brushing using a soft wire loop. Following RPE removal, the choroid was manually detached from the underlying sclera, briefly washed with PBS (21-040-CV; Corning), and then fixed overnight in 4% paraformaldehyde (PFA) at 4°C.

Fixed choroidal tissue was then moved to PBS containing 0.01% NaN_3 and stored at 4°C.

For flow cytometry, choroidal samples were detached from the underlying sclera and then placed in a glass flat bottom 5-ml conical containing ice-cold DMEM with 10% FBS and 25 mM HEPES. At the time of dissociation, collagenase D (11088866001; Millipore Sigma) and dispase II (4942078001; Millipore Sigma) were added to a final concentration of 1% and 0.5%, respectively, and a magnetic micro-stir bar was added. The glass vial was placed in a 37°C water bath, and the sample was allowed to dissociate for 15–20 min with gentle magnetic stirring. Upon completion, the glass vial was placed on ice and 4 ml of ice-cold FACS buffer (PBS containing 5% FBS, 4 mM EDTA [BP2482100; Thermo Fisher Scientific], and 0.09% NaN_3) was added. After passing through a 100-µm filter, the sample was then transferred to a FACS tube and pelleted in a prechilled 4°C centrifuge at 300 G for 5 min. Samples were then decanted, resuspended in cryoprotective media (90% FBS/10% DMSO), transferred to cryotubes, and frozen at −80°C in a Mr. Frosty Freezing Container (5100-0001; Thermo Fisher Scientific). Cryotubes were then transferred to liquid nitrogen for long-term storage.

3D multiplex immunofluorescence: Image capture

To quench autofluorescence and depigment the tissue, choroidal samples underwent three initial rounds of photobleaching in a PBS solution containing a final concentration of 4.5% H_2O_2 (216763; Millipore Sigma) and 20 mM NaOH, using a method adapted from prior work (Du et al., 2019; Meeker et al., 2021, *Preprint*) (Fig. S1). Choroidal tissue was placed in the photobleaching solution in a 12-well culture plate that was sandwiched between two white LED 15,000 lux lights (B09WVNDTLC; Amazon) and incubated for 1 h on an orbital shaker at 4°C. The tissue was then briefly washed in PBS and then photobleached again under the same white light for 1 h at 4°C in a fresh H_2O_2 solution. The tissue was again washed in PBS and then photobleached for a third time in a fresh H_2O_2 solution in a 365-nm ultraviolet LED enclosure (AT8001-D; AlphaThera) for 2 h at 4°C. After photobleaching, the tissue was washed for 1 h at room temperature (RT) in PBS containing 1% BSA. Antigen retrieval was then performed using a citrate-based solution (H-3300-250; Vector Laboratories) that was incubated overnight at 56°C on an orbital shaker. Following antigen retrieval, the tissue samples were washed in PBS containing 1% BSA and blocked for 1 h at RT using Trident Universal Protein Blocking Reagent (GTX30963; GeneTex). The samples were stained overnight at 4°C with primary antibodies diluted in blocking buffer. The following day, the samples were washed, stained with secondary antibodies and Hoechst, and then mounted on microscope slides with Bruch's membrane facing up. Coverslips were mounted using SlowFade Gold Antifade Mountant (S36936; Invitrogen), slides were pressed flat for 15 min, and then imaged on a Nikon AX confocal (Nikon Corporation) at 20× magnification with 30–40 1 µm thick Z-slices.

After the first round of imaging, coverslips were floated off in PBS, and then the slides with the mounted tissues still attached were placed in a standard petri dish containing photobleaching solution. The petri dish was then sandwiched between the two white LED 15,000 lux lights and photobleached for 1 h at 4°C on an orbital shaker, as described previously. Optimization experiments demonstrated that this method was sufficient to completely quench the previous round's fluorophores while leaving the nuclear reference stain intact (Fig. S1), as has been demonstrated previously (Du et al., 2019). Following photobleaching, custom made 3D-printed staining chambers were attached to the microscope slides, creating a seal around the tissue samples and the glass slides. These staining chambers created a removeable enclosed environment for washes and stains, which reduced the volume necessary for staining, eliminated the need for hydrophobic pens, and allowed for a tightly regulated environment. The tissue samples were then reblocked in Trident Universal Protein Blocking Reagent and then stained overnight at 4°C with conjugated primary antibodies diluted in blocking buffer. Unconjugated rabbit antibodies were labeled using FlexAble CoraLite Plus 488 Antibody Labeling Kit (KFA001; ProteinTech) or FlexAble CoraLite Plus 555 Antibody Labeling Kit (KFA002; ProteinTech). The following day, samples were washed, stained with Hoechst, and then new coverslips were mounted using SlowFade Gold Antifade Mountant. Slides were pressed flat for 15 min and then reimaged on a Nikon AX confocal at 20× magnification after slide/stage alignment. This cycle of staining, imaging, and photobleaching was repeated nine times. A complete list of the antibodies used in this study is provided under the Antibodies section.

3D multiplex immunofluorescence: Image analysis

Image tiles were stitched using the NIS-Elements Advanced Research software with the "Optimal Path" and "Fluorescence" options selected. After stitching, the Denoise.ai feature in NIS-Elements was used to enhance image quality. Following this preprocessing, maximum intensity projections were obtained using NIS-Elements, and then the python package VALIS was used to register the maximum intensity projections from each round of staining (Gatenbee et al., 2023). For assembling 3D stacks of registered images, the transformations for each cycle obtained by VALIS on maximum intensity projections were then transferred to the individual Z slices of the respective cycles and then reassembled back into 3D stacks using custom python code. These registered 3D stacks were then cropped to an area of interest using custom python code and then concatenated using ImageJ. 3D volume renderings were obtained from the concatenated 3D stacks using the software package Blender with the tif2blender plugin.

Flow cytometry

For human choroidal flow cytometry, cryopreserved samples were rapidly thawed in a 37°C water bath for 2–3 min, transferred to FACS tubes, and then 4 ml of ice-cold FACS buffer was added. Samples were then pelleted in a prechilled 4°C centrifuge at 300G for 5 min. After decanting, samples were blocked in ice-cold FACS buffer containing 5% True-Stain Monocyte Blocker (426102; BioLegend) and 5% Human TruStain FcX (422301; BioLegend) for 5 min at RT. Conjugated primary antibodies and viability dye (L34975 or L34961; Thermo Fisher Scientific) were diluted in Brilliant Stain Buffer (563794; BD Biosciences) and

then added directly to the sample containing the blocking buffer. Samples were protected from light and stained at 4°C for 30 min. After staining, samples were washed in FACS buffer, pelleted, and then resuspended in Cytofix/Cytoperm Fixation/Permeabilization Solution (554715; BD Biosciences) for 30 min at 4°C. Samples were then washed in the accompanying BD Perm/Wash Buffer and then stained in the same buffer containing 0.02 mM SYTO40 (S11351; Thermo Fisher Scientific) for 30 min on ice. SYTO40, a DNA stain with an excitation/emission profile similar to Brilliant Violet 421, was used to separate nucleated cells from cellular debris. Samples were washed a final time and then resuspended in FACS buffer and analyzed using a spectral-enabled BD FACSymphony A5. Fluorescence minus one controls were used to establish the gating strategy (Fig. S3 A). For flow cytometry on dissociated mouse choroids, the procedure was the same except cells were blocked with Mouse TruStain FcX PLUS (156603; BioLegend) instead of Human TruStain FcX. A complete list of all flow cytometry antibodies is provided, and the mouse choroidal flow cytometry gating scheme is shown (Fig. S3 D).

Lipid metabolism studies

Nile red (N1142; Invitrogen) was dissolved in 100% DMSO at a stock concentration of 0.5 µg/µl and used at a final concentration of 0.005 µg/µl diluted in Trident Universal Protein Blocking Reagent. Choroidal samples were stained overnight at 4°C on a shaker.

Fluorescently labeled LDL (L3482; Invitrogen) was diluted in DMEM (10-013-CMR; Corning) without FBS at a final concentration of 25 µg/ml and then acclimated to 37°C in a cell culture incubator. Freshly isolated choroidal tissue with the RPE removed was then submerged in the solution and incubated for 4 h at 37°C in a cell culture incubator. The tissue samples were then briefly washed in PBS and then fixed overnight at 4°C in 4% PFA. Samples were then washed in PBS containing 1% BSA, blocked with Trident Universal Protein Blocking Reagent, and then stained overnight with primary antibodies at 4°C. The following day, samples were washed, stained with Hoechst, mounted on microscope slides, and imaged.

LC/MS lipidomics was performed on FACS-sorted human choroidal macrophages from cryopreserved tissue digests. 10,000 FOLR2$^+$ macrophages and 10,000 FOLR2$^-$ macrophages were FACS sorted into microcentrifuge tubes containing PBS. Samples were then pelleted, the supernatant was pipetted off, and the cells were immediately flash frozen on liquid nitrogen. Lipid extraction, LC/MS, and analysis of the resulting data were performed by the Molecular Metabolism and Disease Mass Spectrometry Core at Michigan State University.

Mouse choroid dissociation

Eyes were collected and dissected in PBS under a dissecting microscope. Extraocular muscles, connective tissue, and conjunctiva were carefully removed. A puncture was made just below the limbus, and the anterior chamber was removed. The retina was separated from the RPE/choroid, PBS was flushed into the eye cup to remove any remaining neural debris, and the optic nerve was dissected away. The eye cup was washed a final time in PBS and then placed in a glass flat-bottom 5-ml conical containing a magnetic micro-stir bar and ice-cold DMEM with 10% FBS and 25 mM HEPES. The glass vial was then placed in a 37°C water bath and dissociation buffer was added to give a final mixture containing 1% collagenase D, 0.5% dispase II, 1× TrypLE Select (A1217701; Thermo Fisher Scientific), and 10 U/ml DNase I (4716728001; Millipore Sigma). The eye cup was then dissociated for 30 min at 37°C with gentle magnetic stirring. Upon completion, the glass vial was placed on ice and 4 ml of ice-cold FACS buffer was added. After passing through a 100-µm filter, the sample was then transferred to a FACS tube and pelleted in a prechilled 4°C centrifuge at 300G for 5 min.

Topical diphtheria depletion

The base formulation used for topical diphtheria administration was a commercially available lubricating eye drop solution (NDC code 56062-790-01; Publix) containing 0.4% polyethylene glycol 400, 0.3% propylene glycol, aminomethyl propanol, benzalkonium chloride, boric acid, hypromellose, sorbitol, potassium chloride, and sodium chloride. The following penetration enhancers were added to this base formulation: 0.1% Tween-20, 0.1% Tween-80, 0.1% saponin, and 2 mM EDTA. The solution was then sterile filtered, aliquoted, and stored at 4°C. Diphtheria toxin (D0564; Millipore Sigma) was dissolved in PBS at a stock concentration of 1 µg/µl, aliquoted, and stored at −80°C. On the day of administration, diphtheria toxin was thawed and mixed into this customized eye drop formulation with vigorous vortexing at a final concentration of 200 ng/µl. 5 µl was applied daily to each eye.

Mouse ocular imaging and optomotor response test

For fundus and OCT imaging, eyes were dilated with a 1:1 mixture of 1% tropicamide and 2.5% phenylephrine hydrochloride. Mice were anesthetized with 100 mg/kg ketamine and 5 mg/kg xylazine. 2.5% hydroxypropyl methylcellulose (Gonak; Akorn) was applied to each eye, and fundus images were obtained using a Micron IV (Phoenix-Micron). Immediately after fundus imaging, OCT images were obtained using a Bioptigen OCT system (Envisu R-class; Leica Microsystems). A lateral image averaged across 100 B-scans was obtained at the centermost position of the optic nerve head. OCT images were imported to ImageJ, the images were binarized, and a bounding box was drawn across the interface of the RPE/choroid layers. The portion containing the choroid was retained, and the thickness of the choroid to the left and right of the optic nerve, measured at each pixel along the x axis, was obtained. The resulting average of these measurements was used as the average choroidal thickness for each eye.

The optomotor response test was performed as previously described using the software OptoMotry (CerebralMechanics) (Adu-Agyeiwaah et al., 2023). Briefly, mice were placed on a raised platform that was completely enclosed by four computer screens displaying black and white sinusoidal gratings at 100% contrast and 12.0 d/s. A camera placed above the platform was used to monitor head movements in response to changing spatial frequencies of the moving grid. Clockwise grid rotation tested the visual acuity of the left eye, whereas counterclockwise rotation informed the right eye. Maximum visual acuity was

defined as the highest spatial frequency at which tracking occurred.

Laser-induced CNV

For laser-induced CNV, eyes were dilated, and mice were anesthetized as described above. 2.5% hydroxypropyl methylcellulose was applied to a circular coverslip, which was then placed on the eye to be lasered. Mice were positioned in front of an ophthalmic argon green laser (532 nm) coupled to a slit lamp (IRIDEX) with the following settings: power 180 mV, duration 100 ms, and spot size 100 µm. Four laser burns were given per eye (one in each quadrant). 7 days after laser, the mice were euthanized, choroids were fixed with 4% PFA, and the vasculature was stained with Isolectin GS-IB4 (FL-1201-.5; Vector Laboratories). Choroids were then mounted and imaged, and lesion sizes were measured using ImageJ. The average area of the four lesions was used as the final lesion size of each eye.

scRNA-seq

FASTQ files were downloaded from the Gene Expression Omnibus (GEO) database (GEO accessions: GSE203499, GSE230348, GSE210543, GSE135922, GSE149100, GSE183320, and GSE202735) and samples were demultiplexed and aligned using CellRanger Count (Version 7.0.2). The prebuilt human reference transcriptome from 10X Genomics, GRCh38, was used for alignment. CellRanger output files were loaded into Scanpy (Wolf et al., 2018), and the scAR package (Sheng et al., 2022, *Preprint*) from single-cell variational inference (scvi)-tools (Gayoso et al., 2022) was used to identify and remove ambient RNA. To filter out low-quality cells, we used the following thresholds: >300 for total genes, >300 for total counts, and <0.35 for mitochondrial proportion. To identify potential doublets, we used 2 algorithms, Solo (Bernstein et al., 2020), and DoubletDetection (Gayoso and Shor, 2022), and we removed cells that were identified as probable doublets by both. For size factor normalization of the denoised raw counts we used, scranPY (Fortmann, 2023), a package written and maintained by our group, which is a python implementation of r-scran::computeSumFactors (Lun et al., 2016). For dimensionality reduction, we used 3,000 highly variable genes, principal component analysis using 20 components, Harmony for batch correction using individual sample identifiers (Korsunsky et al., 2019), nearest neighbor analysis using 80 neighbors, and Uniform Manifold Approximation and Projection (UMAP) with default parameters. For clustering, we used the Leiden algorithm with a resolution of 0.25 (Traag et al., 2019). Lastly, we removed the RPE cluster, a cluster containing contaminating rods, three other small clusters of unknown origin.

For subclustering of myeloid cells (Fig. S3 C), we subset the data on the CD14$^+$ cluster and then used the scVI model from scvi-tools to compute a latent space representation for dimensionality reduction. We removed one sample from the dataset that contained a large population of unknown cells that did not overlap with the other 98 samples. Cell cycle scores were computed with the Scanpy function score_genes_cell_cycle() using the cell cycle gene list from Tirosh et al. (2016). The denoised expression matrix was used along with three categorical covariates (the individual sample identifier, the donor identifier, and the study identifier) and three continuous covariates (the mitochondrial proportion, the G2M score, and the S score). Nearest neighbors were recomputed using the scVI latent space, and then UMAP was recomputed using default parameters.

DGE analysis was performed on log1p transformed, size factor normalized expression data (scranPY). The R package Seurat (Satija et al., 2015) was used for DGE calculations using the MAST (Finak et al., 2015) implementation of the FindMarkers() function. The following latent variables were used: the donor identifier, log transformed total genes, log transformed total counts, and the mitochondrial proportion. For the comparison of FOLR2$^+$ versus FOLR2$^-$ macrophages, we used only the cells derived from nondiseased samples. Significant genes were defined as those with false discovery rate–corrected P values <0.001 and absolute log fold changes >0.1.

GSEA analysis was performed on the output data from FindMarkers() using the python program GSEApy (Fang et al., 2023). GSEA was done with the prerank() function using LogFC from FindMarkers() output to rank genes. Permutation number was set to 500, minimum size was set to 5, and maximum size was set to 1,000. The following gene sets were downloaded from gsea-msigdb and used for the analyses: Reactome, Hallmark, Wiki, Biocarta, Go-Biological, Go-Cellular, and Go-Molecular.

Bulk RNA-seq

Bulk RNA-seq data were downloaded from the GEO database under accession number GSE135092. Raw-sequencing data are not publicly available. Therefore, we used the precomputed normalized data from Orozco et al. (2020), which was quantified using HTSeqGenie as reads per kilobase of gene model per million total reads and normalized by size factors computed using DESeq2 (Love et al., 2014).

Antibodies

The antibodies used in this study were: PE anti-CD3 (UCHT1) (300407; BioLegend), PE anti-NKp46 (9E2) (331907; BioLegend), APC anti-CD19 (HIB19) (302211; BioLegend), BV785 anti-CD11b (M1/70) (101243; BioLegend), BUV805 anti-CD117 (104D2) (749481; BD Biosciences), FITC anti-CD11c (Bu15) (337213; BioLegend), PE anti-CD83 (HB15e) (305307; BioLegend), PE/Cy7 anti-CD52 (HI186) (316011; BioLegend), anti-LYVE1 (EPR21857) (ab219556; Abcam), APC/Cy7 anti-FOLR2 (94b/FOLR2) (391702; BioLegend), BUV395 anti-CCR2 (1D9) (747854; BD Biosciences), BUV615 anti-CD45 (HI30) (751472; BD Biosciences), BUV737 anti-CD64 (10.1) (612777; BD Biosciences), AF647 anti-rabbit (A-31573; Thermo Fisher Scientific), BV650 anti-LY6C (HK1.4) (128049; BioLegend), BV785 anti–I-A/I-E (M5/114.15.2) (107645; BioLegend), APC anti-FOLR2 (10/FR2) (153305; BioLegend), PE anti-FOLR2 (10/FR2) (153303; BioLegend), APC anti-CD11c (N418) (117309; BioLegend), AF700 anti-CD45 (30-F11) (103127; BioLegend), BUV395 anti-F4/80 (BM8) (363–4801-82; Invitrogen), BUV496 anti-CD11a (M17/4) (741071; BD Biosciences), BUV615 anti-CD11b (M1/70) (366–0112-82; Invitrogen), BUV805 anti-LY6G (1A8) (741994; BD Biosciences), anti-IL1B (3A6) (12242S; Cell Signaling), anti-FOLR2 (EPR25731-70) (ab302532; Abcam), AF647 anti-IBA1 (EPR16588) (ab225261; Abcam), AF546 anti-

rabbit (A10040; Thermo Fisher Scientific), AF488 anti-mouse (A-21202; Thermo Fisher Scientific), AF488 anti-CD11c (D3V1E) (95103S; Cell Signaling), PE anti-FCER1A (AER-37) (334609; BioLegend), AF488 anti-CD14 (D7A2T) (37518S; Cell Signaling), Coralite 488 anti-LYVE1 (EPR21857) (ab219556; Abcam), AF647 anti-CD45 (HI30) (304020; BioLegend), AF647 anti-TUBB3 (AA10) (657405; BioLegend), FITC anti–UEA-Lectin (L32476; Invitrogen), AF555 anti-PLP1 (EPR23504-106) (ab313220; Abcam), PE anti-PDPN (NC-08) (337003; BioLegend), AF647 anti-SMA (1A4) (sc-32251 AF647; Santa Cruz), Coralite 488 anti-VEGFA (EP1176Y) (ab52917; Abcam), Coralite 555 anti-MLANA (E9Q4O) (64718S; Cell Signaling), True-Stain Monocyte Blocker (426102; BioLegend), Mouse TruStain FcX anti-CD16/32 (93) (101319; BioLegend), Mouse TruStain FcX PLUS anti-CD16/32 (S17011E) (156603; BioLegend), and Human TruStain FcX (422301; BioLegend).

Statistical analyses

Statistical tests were performed using GraphPad Prism (version 6.01). Sample sizes and statistical tests are listed in the figure legends. Data were visualized using the R package ggplot2. Correction for multiple hypothesis testing was applied where indicated.

Online supplemental material

Fig. S1, related to Figs. 1 and 2 and Fig. 6, shows the microscope images of human choroid before and after autofluorescence quenching, depigmentation, and fluorophore bleaching per the 3D multiplex immunofluorescence protocol. Fig. S2, related to Figs. 1, 2, 3, and 6, shows the ex vivo fundus and OCT imaging of human donor eyes. Fig. S3 shows the human and mouse flow cytometry gating schemes, fluorescence minus one controls, and scRNA-seq marker genes of myeloid subclusters. Fig. S4, related to Fig. 3, shows the various endpoint measurements in FOLR2^{-} macrophages from AMD versus non-diseased choroids. Fig. S5, related to Figs. 5 and 6, shows the diphtheria toxin control experiments. Table S1 shows the characteristics of each eye donor. Table S2 shows the ex vivo ocular imaging findings per eye.

Data availability

Raw scRNA-seq data (FASTQ format) are available from the NCBI-SRA repositories of the original depositing authors (GEO accessions: GSE203499, GSE230348, GSE210543, GSE135922, GSE149100, GSE183320, and GSE202735). Processed Scanpy (.H5AD) and Seurat (.RDS) files from this data have been deposited under GEO accession GSE291614. Bulk RNA-seq data are available under accession number GSE135092 per the original depositing authors.

Acknowledgments

The authors would like to acknowledge the UAB Core Grant for Vision Research, P30-EY003039, the Carl G. and Pauline Buck Trust, and the UAB Flow Cytometry & Single Cell Core Facility, supported by the Center for AIDS Research, AI027767, and the O'Neal Comprehensive Cancer Center, CA013148.

S.D. Fortmann is supported by the National Eye Institute (NEI), National Institutes of Health (NIH) F30EY033198. B.F. Frey is supported by National Institute of Diabetes and Digestive and Kidney Diseases (NIDDK), NIH F30DK127865. R.F. Rosencrans is supported by NIDDK, NIH F30DK131911. M.B. Grant is supported by NEI, NIH R01EY035539, R01EY012601, R01EY033620, R01EY032753, and R01EY025383.

Author contributions: S.D. Fortmann: conceptualization, data curation, formal analysis, investigation, methodology, project administration, software, validation, visualization, and writing—original draft, review, and editing. B.F. Frey: data curation and writing—review and editing. R.F. Rosencrans: investigation and writing—review and editing. Y. Adu-Rutledge: investigation. E. Ready V: project administration and resources. K.V. Kilchrist: conceptualization, project administration, and resources. R.S. Welner: resources and writing—review and editing. M.E. Boulton: supervision and writing—review and editing. D.R. Saban: conceptualization, methodology, and writing—original draft, review, and editing. M.B. Grant: conceptualization, data curation, formal analysis, funding acquisition, project administration, resources, supervision, and writing—review and editing.

Disclosures: K.V. Kilchrist reported personal fees from Kodiak Sciences Inc. during the conduct of the study. No other disclosures were reported.

Submitted: 28 October 2024
Revised: 2 February 2025
Accepted: 24 March 2025

References

Adu-Agyeiwaah, Y., C.P. Vieira, B. Asare-Bediako, S. Li Calzi, M. DuPont, J. Floyd, S. Boye, V. Chiodo, J.V. Busik, and M.B. Grant. 2023. Intravitreal administration of AAV2-SIRT1 reverses diabetic retinopathy in a mouse model of type 2 diabetes. *Transl. Vis. Sci. Technol.* 12:20. https://doi.org/10.1167/tvst.12.4.20

Alm, A., and A. Bill. 1972. The oxygen supply to the retina. II. Effects of high intraocular pressure and of increased arterial carbon dioxide tension on uveal and retinal blood flow in cats. A study with radioactively labelled microspheres including flow determinations in brain and some other tissues. *Acta Physiol. Scand.* 84:306–319. https://doi.org/10.1111/j.1748-1716.1972.tb05182.x

Ambati, J., A. Anand, S. Fernandez, E. Sakurai, B.C. Lynn, W.A. Kuziel, B.J. Rollins, and B.K. Ambati. 2003. An animal model of age-related macular degeneration in senescent Ccl-2- or Ccr-2-deficient mice. *Nat. Med.* 9:1390–1397. https://doi.org/10.1038/nm950

Ames, A. III, Y.Y. Li, E.C. Heher, and C.R. Kimble. 1992. Energy metabolism of rabbit retina as related to function: High cost of Na^+ transport. *J. Neurosci.* 12:840–853. https://doi.org/10.1523/JNEUROSCI.12-03-00840.1992

Anquetil, C., J.-E. Salem, B. Lebrun-Vignes, S. Touhami, A.-C. Desbois, G. Maalouf, F. Domont, Y. Allenbach, P. Cacoub, B. Bodaghi, and D. Saadoun. 2020. Evolving spectrum of drug-induced uveitis at the era of immune checkpoint inhibitors results from the WHO's pharmacovigilance database. *J. Autoimmun.* 111:102454. https://doi.org/10.1016/j.jaut.2020.102454

Baudouin, C., D. Fredj-Reygrobellet, P. Gastaud, and P. Lapalus. 1988. HLA DR and DQ distribution in normal human ocular structures. *Curr. Eye Res.* 7:903–911. https://doi.org/10.3109/02713688808997247

Bernstein, N.J., N.L. Fong, I. Lam, M.A. Roy, D.G. Hendrickson, and D.R. Kelley. 2020. Solo: Doublet identification in single-cell RNA-seq via semi-supervised deep learning. *Cell Syst.* 11:95–101.e5. https://doi.org/10.1016/j.cels.2020.05.010

Brown, D.M., P.K. Kaiser, M. Michels, G. Soubrane, J.S. Heier, R.Y. Kim, J.P. Sy, S. Schneider, and ANCHOR Study Group. 2006. Ranibizumab versus verteporfin for neovascular age-related macular degeneration. *N. Engl. J. Med.* 355:1432–1444. https://doi.org/10.1056/NEJMoa062655

Campochiaro, P.A. 2015. Molecular pathogenesis of retinal and choroidal vascular diseases. *Prog. Retin. Eye Res.* 49:67–81. https://doi.org/10.1016/j.preteyeres.2015.06.002

Caspi, R.R. 2006. Ocular autoimmunity: The price of privilege? *Immunol. Rev.* 213:23–35. https://doi.org/10.1111/j.1600-065X.2006.00439.x

Cherepanoff, S., P. McMenamin, M.C. Gillies, E. Kettle, and S.H. Sarks. 2010. Bruch's membrane and choroidal macrophages in early and advanced age-related macular degeneration. *Br. J. Ophthalmol.* 94:918–925. https://doi.org/10.1136/bjo.2009.165563

Collin, J., M.S.R. Hasoon, D. Zerti, S. Hammadi, B. Dorgau, L. Clarke, D. Steel, R. Hussain, J. Coxhead, S. Lisgo, et al. 2023. Single-cell RNA sequencing reveals transcriptional changes of human choroidal and retinal pigment epithelium cells during fetal development, in healthy adult and intermediate age-related macular degeneration. *Hum. Mol. Genet.* 32:1698–1710. https://doi.org/10.1093/hmg/ddad007

Curcio, C.A., M. Johnson, M. Rudolf, and J.D. Huang. 2011. The oil spill in ageing Bruch membrane. *Br. J. Ophthalmol.* 95:1638–1645. https://doi.org/10.1136/bjophthalmol-2011-300344

Damato, B., A. Eleuteri, A.F. Taktak, and S.E. Coupland. 2011. Estimating prognosis for survival after treatment of choroidal melanoma. *Prog. Retin. Eye Res.* 30:285–295. https://doi.org/10.1016/j.preteyeres.2011.05.003

de Paiva, C.S., A.J. St Leger, and R.R. Caspi. 2022. Mucosal immunology of the ocular surface. *Mucosal Immunol.* 15:1143–1157. https://doi.org/10.1038/s41385-022-00551-6

Dick, S.A., A. Wong, H. Hamidzada, S. Nejat, R. Nechanitzky, S. Vohra, B. Mueller, R. Zaman, C. Kantores, L. Aronoff, et al. 2022. Three tissue resident macrophage subsets coexist across organs with conserved origins and life cycles. *Sci. Immunol.* 7:eabf7777. https://doi.org/10.1126/sciimmunol.abf7777

Droho, S., A. Rajesh, C.M. Cuda, H. Perlman, and J.A. Lavine. 2023. CD11c+ macrophages are proangiogenic and necessary for experimental choroidal neovascularization. *JCI Insight.* 8:e168142. https://doi.org/10.1172/jci.insight.168142

Du, Z., J.R. Lin, R. Rashid, Z. Maliga, S. Wang, J.C. Aster, B. Izar, P.K. Sorger, and S. Santagata. 2019. Qualifying antibodies for image-based immune profiling and multiplexed tissue imaging. *Nat. Protoc.* 14:2900–2930. https://doi.org/10.1038/s41596-019-0206-y

Espinosa-Heidmann, D.G., I.J. Suner, E.P. Hernandez, D. Monroy, K.G. Csaky, and S.W. Cousins. 2003. Macrophage depletion diminishes lesion size and severity in experimental choroidal neovascularization. *Invest. Ophthalmol. Vis. Sci.* 44:3586–3592. https://doi.org/10.1167/iovs.03-0038

Fang, Z., X. Liu, and G. Peltz. 2023. GSEApy: A comprehensive package for performing gene set enrichment analysis in Python. *Bioinformatics*. 39:btac757. https://doi.org/10.1093/bioinformatics/btac757

Finak, G., A. McDavid, M. Yajima, J. Deng, V. Gersuk, A.K. Shalek, C.K. Slichter, H.W. Miller, M.J. McElrath, M. Prlic, et al. 2015. MAST: A flexible statistical framework for assessing transcriptional changes and characterizing heterogeneity in single-cell RNA sequencing data. *Genome Biol.* 16:278. https://doi.org/10.1186/s13059-015-0844-5

Fortmann, S. 2023. sfortma2/scranPY: A python implementation of r-scran: computeSumFactors, normalization by deconvolution for single-cell RNA-sequencing (v1.1). *Zenodo*. https://doi.org/10.5281/zenodo.10072109

Fritsche, L.G., W. Igl, J.N. Bailey, F. Grassmann, S. Sengupta, J.L. Bragg-Gresham, K.P. Burdon, S.J. Hebbring, C. Wen, M. Gorski, et al. 2016. A large genome-wide association study of age-related macular degeneration highlights contributions of rare and common variants. *Nat. Genet.* 48:134–143. https://doi.org/10.1038/ng.3448

Gatenbee, C.D., A.M. Baker, S. Prabhakaran, O. Swinyard, R.J.C. Slebos, G. Mandal, E. Mulholland, N. Andor, A. Marusyk, S. Leedham, et al. 2023. Virtual alignment of pathology image series for multi-gigapixel whole slide images. *Nat. Commun.* 14:4502. https://doi.org/10.1038/s41467-023-40218-9

Gayoso, A., R. Lopez, G. Xing, P. Boyeau, V. Valiollah Pour Amiri, J. Hong, K. Wu, M. Jayasuriya, E. Mehlman, M. Langevin, et al. 2022. A Python library for probabilistic analysis of single-cell omics data. *Nat. Biotechnol.* 40:163–166. https://doi.org/10.1038/s41587-021-01206-w

Gayoso, A., and J. Shor. 2022. Jonathanshor/doubletdetection: Doubletdetection V4.2. *Zenodo*. https://doi.org/10.5281/zenodo.2678041

Heier, J.S., D.M. Brown, V. Chong, J.-F. Korobelnik, P.K. Kaiser, Q.D. Nguyen, B. Kirchhof, A. Ho, Y. Ogura, G.D. Yancopoulos, et al. 2012. Intravitreal aflibercept (VEGF trap-eye) in wet age-related macular degeneration. *Ophthalmology*. 119:2537–2548. https://doi.org/10.1016/j.ophtha.2012.09.006

Hoang, Q.V., R.A. Linsenmeier, C.K. Chung, and C.A. Curcio. 2002. Photoreceptor inner segments in monkey and human retina: Mitochondrial density, optics, and regional variation. *Vis. Neurosci.* 19:395–407. https://doi.org/10.1017/S0952523802194028

Jia, Y., S.T. Bailey, D.J. Wilson, O. Tan, M.L. Klein, C.J. Flaxel, B. Potsaid, J.J. Liu, C.D. Lu, M.F. Kraus, et al. 2014. Quantitative optical coherence tomography angiography of choroidal neovascularization in age-related macular degeneration. *Ophthalmology*. 121:1435–1444. https://doi.org/10.1016/j.ophtha.2014.01.034

Joyal, J.S., Y. Sun, M.L. Gantner, Z. Shao, L.P. Evans, N. Saba, T. Fredrick, S. Burnim, J.S. Kim, G. Patel, et al. 2016. Retinal lipid and glucose metabolism dictates angiogenesis through the lipid sensor Ffar1. *Nat. Med.* 22:439–445. https://doi.org/10.1038/nm.4059

Killingsworth, M.C., J.P. Sarks, and S.H. Sarks. 1990. Macrophages related to Bruch's membrane in age-related macular degeneration. *Eye*. 4:613–621. https://doi.org/10.1038/eye.1990.86

Korsunsky, I., N. Millard, J. Fan, K. Slowikowski, F. Zhang, K. Wei, Y. Baglaenko, M. Brenner, P.R. Loh, and S. Raychaudhuri. 2019. Fast, sensitive and accurate integration of single-cell data with Harmony. *Nat. Methods*. 16:1289–1296. https://doi.org/10.1038/s41592-019-0619-0

Lambert, V., J. Lecomte, S. Hansen, S. Blacher, M.-L.A. Gonzalez, I. Struman, N.E. Sounni, E. Rozet, P. de Tullio, J.M. Foidart, et al. 2013. Laser-induced choroidal neovascularization model to study age-related macular degeneration in mice. *Nat. Protoc.* 8:2197–2211. https://doi.org/10.1038/nprot.2013.135

Lejoyeux, R., J. Benillouche, J. Ong, M.H. Errera, E.A. Rossi, S.R. Singh, K.K. Dansingani, S. da Silva, D. Sinha, J.A. Sahel, et al. 2022. Choriocapillaris: Fundamentals and advancements. *Prog. Retin. Eye Res.* 87:100997. https://doi.org/10.1016/j.preteyeres.2021.100997

Lewandowski, D., C.L. Sander, A. Tworak, F. Gao, Q. Xu, and D. Skowronska-Krawczyk. 2022. Dynamic lipid turnover in photoreceptors and retinal pigment epithelium throughout life. *Prog. Retin. Eye Res.* 89:101037. https://doi.org/10.1016/j.preteyeres.2021.101037

Li, C.M., B.H. Chung, J.B. Presley, G. Malek, X. Zhang, N. Dashti, L. Li, J. Chen, K. Bradley, H.S. Kruth, and C.A. Curcio. 2005a. Lipoprotein-like particles and cholesteryl esters in human Bruch's membrane: Initial characterization. *Invest. Ophthalmol. Vis. Sci.* 46:2576–2586. https://doi.org/10.1167/iovs.05-0034

Li, C.M., J.B. Presley, X. Zhang, N. Dashti, B.H. Chung, N.E. Medeiros, C. Guidry, and C.A. Curcio. 2005b. Retina expresses microsomal triglyceride transfer protein: Implications for age-related maculopathy. *J. Lipid Res.* 46:628–640. https://doi.org/10.1194/jlr.M400428-JLR200

Liu, X., S. Chen, H. Leng, Y. Wang, Y. Liu, Y. Shen, S. Liu, H. Yi, J. Li, and J. Zhong. 2023. New findings on choroidal features in healthy people by ultra-widefield swept-source optical coherence tomography angiography. *Sci. Rep.* 13:9215. https://doi.org/10.1038/s41598-023-36374-z

Liu, Z., Y. Gu, S. Chakarov, C. Bleriot, I. Kwok, X. Chen, A. Shin, W. Huang, R.J. Dress, C.A. Dutertre, et al. 2019. Fate mapping via Ms4a3-expression history traces monocyte-derived cells. *Cell*. 178:1509–1525.e19. https://doi.org/10.1016/j.cell.2019.08.009

Lopez, P.F., H.M. Lambert, H.E. Grossniklaus, and P. Sternberg Jr. 1993. Well-defined subfoveal choroidal neovascular membranes in age-related macular degeneration. *Ophthalmology*. 100:415–422. https://doi.org/10.1016/S0161-6420(93)31657-X

Love, M.I., W. Huber, and S. Anders. 2014. Moderated estimation of fold change and dispersion for RNA-seq data with DESeq2. *Genome Biol.* 15:550. https://doi.org/10.1186/s13059-014-0550-8

Lun, A.T., K. Bach, and J.C. Marioni. 2016. Pooling across cells to normalize single-cell RNA sequencing data with many zero counts. *Genome Biol.* 17:75. https://doi.org/10.1186/s13059-016-0947-7

Lutty, G.A., D.S. McLeod, I.A. Bhutto, M.M. Edwards, and J.M. Seddon. 2020. Choriocapillaris dropout in early age-related macular degeneration. *Exp. Eye Res.* 192:107939. https://doi.org/10.1016/j.exer.2020.107939

Masson, D., X.C. Jiang, L. Lagrost, and A.R. Tall. 2009. The role of plasma lipid transfer proteins in lipoprotein metabolism and atherogenesis. *J. Lipid Res.* 50:S201–S206. https://doi.org/10.1194/jlr.R800061-JLR200

McLeod, D.S., I. Bhutto, M.M. Edwards, R.E. Silver, J.M. Seddon, and G.A. Lutty. 2016. Distribution and quantification of choroidal macrophages in human eyes with age-related macular degeneration. *Invest. Ophthalmol. Vis. Sci.* 57:5843–5855. https://doi.org/10.1167/iovs.16-20049

McLeod, D.S., R. Grebe, I. Bhutto, C. Merges, T. Baba, and G.A. Lutty. 2009. Relationship between RPE and choriocapillaris in age-related macular

degeneration. *Invest. Ophthalmol. Vis. Sci.* 50:4982–4991. https://doi.org/10.1167/iovs.09-3639

McLeod, D.S., and G.A. Lutty. 1994. High-resolution histologic analysis of the human choroidal vasculature. *Invest. Ophthalmol. Vis. Sci.* 35:3799–3811.

McMenamin, P.G., D.R. Saban, and S.J. Dando. 2019. Immune cells in the retina and choroid: Two different tissue environments that require different defenses and surveillance. *Prog. Retin. Eye Res.* 70:85–98. https://doi.org/10.1016/j.preteyeres.2018.12.002

McMenamin, P.G., G.T. Shields, Y. Seyed-Razavi, H. Kalirai, R.H. Insall, L.M. Machesky, and S.E. Coupland. 2020. Melanoblasts populate the mouse choroid earlier in development than previously described. *Invest. Ophthalmol. Vis. Sci.* 61:33. https://doi.org/10.1167/iovs.61.10.33

Meeker, A.K., C.M. Heaphy, C.M. Davis, S. Roy, and E.A. Platz. 2021. Photochemical pre-bleaching of formalin-fixed archival prostate tissues significantly reduces autofluorescence to facilitate multiplex immunofluorescence staining. *bioRxiv*. https://doi.org/10.1101/2021.11.09.467916 (Preprint posted November 11, 2021).

Messinger, J.D., M. Brinkmann, J.A. Kimble, A. Berlin, K.B. Freund, G.H. Grossman, T. Ach, and C.A. Curcio. 2023. Ex vivo OCT-based multimodal imaging of human donor eyes for research into age-related macular degeneration. *J. Vis. Exp.*:65240. https://doi.org/10.3791/65240

Mullin, N.K., A.P. Voigt, M.J. Flamme-Wiese, X. Liu, M.J. Riker, K. Varzavand, E.M. Stone, B.A. Tucker, and R.F. Mullins. 2023. Multimodal single-cell analysis of nonrandom heteroplasmy distribution in human retinal mitochondrial disease. *JCI Insight*. 8:e165937. https://doi.org/10.1172/jci.insight.165937

Mullins, R.F., M.N. Johnson, E.A. Faidley, J.M. Skeie, and J. Huang. 2011. Choriocapillaris vascular dropout related to density of drusen in human eyes with early age-related macular degeneration. *Invest. Ophthalmol. Vis. Sci.* 52:1606–1612. https://doi.org/10.1167/iovs.10-6476

Nakashima-Matsushita, N., T. Homma, S. Yu, T. Matsuda, N. Sunahara, T. Nakamura, M. Tsukano, M. Ratnam, and T. Matsuyama. 1999. Selective expression of folate receptor beta and its possible role in methotrexate transport in synovial macrophages from patients with rheumatoid arthritis. *Arthritis Rheum.* 42:1609–1616. https://doi.org/10.1002/1529-0131(199908)42:8<1609::AID-ANR7>3.0.CO;2-L

Nawaz, F.Z., and E.T. Kipreos. 2022. Emerging roles for folate receptor FOLR1 in signaling and cancer. *Trends Endocrinol. Metab.* 33:159–174. https://doi.org/10.1016/j.tem.2021.12.003

Niederkorn, J.Y., and J. Stein-Streilein. 2010. History and physiology of immune privilege. *Ocul. Immunol. Inflamm.* 18:19–23. https://doi.org/10.3109/09273940903564766

O'Koren, E.G., C. Yu, M. Klingeborn, A.Y.W. Wong, C.L. Prigge, R. Mathew, J. Kalnitsky, R.A. Msallam, A. Silvin, J.N. Kay, et al. 2019. Microglial function is distinct in different anatomical locations during retinal homeostasis and degeneration. *Immunity*. 50:723–737.e7. https://doi.org/10.1016/j.immuni.2019.02.007

Okawa, H., A.P. Sampath, S.B. Laughlin, and G.L. Fain. 2008. ATP consumption by mammalian rod photoreceptors in darkness and in light. *Curr. Biol.* 18:1917–1921. https://doi.org/10.1016/j.cub.2008.10.029

Olsen, T.W., and X. Feng. 2004. The Minnesota Grading System of eye bank eyes for age-related macular degeneration. *Invest. Ophthalmol. Vis. Sci.* 45:4484–4490. https://doi.org/10.1167/iovs.04-0342

Orozco, L.D., H.H. Chen, C. Cox, K.J. Katschke Jr., R. Arceo, C. Espiritu, P. Caplazi, S.S. Nghiem, Y.J. Chen, Z. Modrusan, et al. 2020. Integration of eQTL and a single-cell atlas in the human eye identifies causal genes for age-related macular degeneration. *Cell Rep.* 30:1246–1259.e6. https://doi.org/10.1016/j.celrep.2019.12.082

Pan, W.W., T.J. Wubben, and C.G. Besirli. 2021. Photoreceptor metabolic reprogramming: Current understanding and therapeutic implications. *Commun. Biol.* 4:245. https://doi.org/10.1038/s42003-021-01765-3

Penfold, P., M. Killingsworth, and S. Sarks. 1984. An ultrastructural study of the role of leucocytes and fibroblasts in the breakdown of Bruch's membrane. *Aust. J. Ophthalmol.* 12:23–31. https://doi.org/10.1111/j.1442-9071.1984.tb01120.x

Penfold, P.L., M.C. Killingsworth, and S.H. Sarks. 1985. Senile macular degeneration: The involvement of immunocompetent cells. *Graefes Arch. Clin. Exp. Ophthalmol.* 223:69–76. https://doi.org/10.1007/BF02150948

Pennesi, M.E., M. Neuringer, and R.J. Courtney. 2012. Animal models of age related macular degeneration. *Mol. Aspects Med.* 33:487–509. https://doi.org/10.1016/j.mam.2012.06.003

Puig-Kröger, A., E. Sierra-Filardi, A. Domínguez-Soto, R. Samaniego, M.T. Corcuera, F. Gómez-Aguado, M. Ratnam, P. Sánchez-Mateos, and A.L. Corbí. 2009. Folate receptor β is expressed by tumor-associated macrophages and constitutes a marker for M2 anti-inflammatory/regulatory macrophages. *Cancer Res.* 69:9395–9403. https://doi.org/10.1158/0008-5472.CAN-09-2050

Ramos, R.N., Y. Missolo-Koussou, Y. Gerber-Ferder, C.P. Bromley, M. Bugatti, N.G. Núñez, J.T. Boari, W. Richer, L. Menger, and J. Denizeau. 2022. Tissue-resident FOLR2$^+$ macrophages associate with CD8$^+$ T cell infiltration in human breast cancer. *Cell*. 185:1189–1207.e25. https://doi.org/10.1016/j.cell.2022.02.021

Reiner, A., M.E.C. Fitzgerald, N. Del Mar, and C. Li. 2018. Neural control of choroidal blood flow. *Prog. Retin. Eye Res.* 64:96–130. https://doi.org/10.1016/j.preteyeres.2017.12.001

Reyes-Reveles, J., A. Dhingra, D. Alexander, A. Bragin, N.J. Philp, and K. Boesze-Battaglia. 2017. Phagocytosis-dependent ketogenesis in retinal pigment epithelium. *J. Biol. Chem.* 292:8038–8047. https://doi.org/10.1074/jbc.M116.770784

Rosenfeld, P.J., D.M. Brown, J.S. Heier, D.S. Boyer, P.K. Kaiser, C.Y. Chung, R.Y. Kim, and MARINA Study Group. 2006. Ranibizumab for neovascular age-related macular degeneration. *N. Engl. J. Med.* 355:1419–1431. https://doi.org/10.1056/NEJMoa054481

Saishin, Y., Y. Saishin, K. Takahashi, R. Lima e Silva, D. Hylton, J.S. Rudge, S.J. Wiegand, and P.A. Campochiaro. 2003. VEGF-TRAP(R1R2) suppresses choroidal neovascularization and VEGF-induced breakdown of the blood-retinal barrier. *J. Cell. Physiol.* 195:241–248. https://doi.org/10.1002/jcp.10246

Sakurai, E., A. Anand, B.K. Ambati, N. van Rooijen, and J. Ambati. 2003. Macrophage depletion inhibits experimental choroidal neovascularization. *Invest. Ophthalmol. Vis. Sci.* 44:3578–3585. https://doi.org/10.1167/iovs.03-0097

Samaniego, R., B.S. Palacios, Á. Domiguez-Soto, C. Vidal, A. Salas, T. Matsuyama, C. Sánchez-Torres, I. de la Torre, M.E. Miranda-Carús, P. Sánchez-Mateos, and A. Puig-Kröger. 2014. Macrophage uptake and accumulation of folates are polarization-dependent in vitro and in vivo and are regulated by activin A. *J. Leukoc. Biol.* 95:797–808. https://doi.org/10.1189/jlb.0613345

Santos, A.M., R. Calvente, M. Tassi, M.C. Carrasco, D. Martín-Oliva, J.L. Marín-Teva, J. Navascués, and M.A. Cuadros. 2008. Embryonic and postnatal development of microglial cells in the mouse retina. *J. Comp. Neurol.* 506:224–239. https://doi.org/10.1002/cne.21538

Sarks, J.P., S.H. Sarks, and M.C. Killingsworth. 1997. Morphology of early choroidal neovascularisation in age-related macular degeneration: Correlation with activity. *Eye*. 11:515–522. https://doi.org/10.1038/eye.1997.137

Satija, R., J.A. Farrell, D. Gennert, A.F. Schier, and A. Regev. 2015. Spatial reconstruction of single-cell gene expression data. *Nat. Biotechnol.* 33:495–502. https://doi.org/10.1038/nbt.3192

Sennlaub, F., C. Auvynet, B. Calippe, S. Lavalette, L. Poupel, S.J. Hu, E. Dominguez, S. Camelo, O. Levy, E. Guyon, et al. 2013. CCR2(+) monocytes infiltrate atrophic lesions in age-related macular disease and mediate photoreceptor degeneration in experimental subretinal inflammation in Cx3cr1 deficient mice. *EMBO Mol. Med.* 5:1775–1793. https://doi.org/10.1002/emmm.201302692

Sharma, A., J.J.W. Seow, C.A. Dutertre, R. Pai, C. Blériot, A. Mishra, R.M.M. Wong, G.S.N. Singh, S. Sudhagar, S. Khalilnezhad, et al. 2020. Onco-fetal reprogramming of endothelial cells drives immunosuppressive macrophages in hepatocellular carcinoma. *Cell*. 183:377–394.e21. https://doi.org/10.1016/j.cell.2020.08.040

Sheng, C., R. Lopes, G. Li, S. Schuierer, A. Waldt, R. Cuttat, S. Dimitrieva, A. Kauffmann, E. Durand, and G.G. Galli. 2022. Probabilistic machine learning ensures accurate ambient denoising in droplet-based single-cell omics. *bioRxiv*. https://doi.org/10.1101/2022.01.14.476312 (Preprint posted March 24, 2022).

Tan, X., K. Fujiu, I. Manabe, J. Nishida, R. Yamagishi, Y. Terashima, K. Matsushima, T. Kaburaki, R. Nagai, and Y. Yanagi. 2016. Choroidal neovascularization is inhibited in splenic-denervated or splenectomized mice with a concomitant decrease in intraocular macrophage. *PLoS One*. 11:e0160985. https://doi.org/10.1371/journal.pone.0160985

Thibault, T., I. Ben Ghezala, R. Freppel, A. Rajillah, C. Boulay, P. Brunel, M. Atzenhoffer, C. Auvens, H. Devilliers, and A. Grandvuillemin. 2024. Drug-induced uveitis related to checkpoint inhibitors and MAP-kinase inhibitors. *Ophthalmology*. 131:249–251. https://doi.org/10.1016/j.ophtha.2023.10.004

Tirosh, I., B. Izar, S.M. Prakadan, M.H. Wadsworth II, D. Treacy, J.J. Trombetta, A. Rotem, C. Rodman, C. Lian, G. Murphy, et al. 2016. Dissecting the multicellular ecosystem of metastatic melanoma by single-cell RNA-seq. *Science*. 352:189–196. https://doi.org/10.1126/science.aad0501

Traag, V.A., L. Waltman, and N.J. van Eck. 2019. From louvain to leiden: Guaranteeing well-connected communities. *Sci. Rep.* 9:5233. https://doi.org/10.1038/s41598-019-41695-z

Tsutsumi, C., K.-H. Sonoda, K. Egashira, H. Qiao, T. Hisatomi, S. Nakao, M. Ishibashi, I.F. Charo, T. Sakamoto, T. Murata, and T. Ishibashi. 2003. The critical role of ocular-infiltrating macrophages in the development of choroidal neovascularization. *J. Leukoc. Biol.* 74:25–32. https://doi.org/10.1189/jlb.0902436

Voigt, A.P., K. Mulfaul, N.K. Mullin, M.J. Flamme-Wiese, J.C. Giacalone, E.M. Stone, B.A. Tucker, T.E. Scheetz, and R.F. Mullins. 2019. Single-cell transcriptomics of the human retinal pigment epithelium and choroid in health and macular degeneration. *Proc. Natl. Acad. Sci. USA.* 116: 24100–24107. https://doi.org/10.1073/pnas.1914143116

Voigt, A.P., N.K. Mullin, K. Mulfaul, L.P. Lozano, L.A. Wiley, M.J. Flamme-Wiese, E.A. Boese, I.C. Han, T.E. Scheetz, E.M. Stone, et al. 2022. Choroidal endothelial and macrophage gene expression in atrophic and neovascular macular degeneration. *Hum. Mol. Genet.* 31:2406–2423. https://doi.org/10.1093/hmg/ddac043

Voigt, A.P., S.S. Whitmore, K. Mulfaul, K.R. Chirco, J.C. Giacalone, M.J. Flamme-Wiese, A. Stockman, E.M. Stone, B.A. Tucker, T.E. Scheetz, and R.F. Mullins. 2020. Bulk and single-cell gene expression analyses reveal aging human choriocapillaris has pro-inflammatory phenotype. *Microvasc. Res.* 131:104031. https://doi.org/10.1016/j.mvr.2020.104031

Wang, L., C.M. Li, M. Rudolf, O.V. Belyaeva, B.H. Chung, J.D. Messinger, N.Y. Kedishvili, and C.A. Curcio. 2009. Lipoprotein particles of intraocular origin in human Bruch membrane: An unusual lipid profile. *Invest. Ophthalmol. Vis. Sci.* 50:870–877. https://doi.org/10.1167/iovs.08-2376

Wolf, F.A., P. Angerer, and F.J. Theis. 2018. SCANPY: Large-scale single-cell gene expression data analysis. *Genome Biol.* 19:15. https://doi.org/10.1186/s13059-017-1382-0

Wong, W.L., X. Su, X. Li, C.M. Cheung, R. Klein, C.Y. Cheng, and T.Y. Wong. 2014. Global prevalence of age-related macular degeneration and disease burden projection for 2020 and 2040: A systematic review and meta-analysis. *Lancet Glob. Health.* 2:e106–e116. https://doi.org/10.1016/S2214-109X(13)70145-1

Wu, M., E.L. Fletcher, H.R. Chinnery, L.E. Downie, and S.N. Mueller. 2024. Redefining our vision: An updated guide to the ocular immune system. *Nat. Rev. Immunol.* 24:896–911. https://doi.org/10.1038/s41577-024-01064-y

Yang, X., L. Zhao, M.M. Campos, M. Abu-Asab, D. Ortolan, N. Hotaling, K. Bharti, and W.T. Wong. 2020. CSF1R blockade induces macrophage ablation and results in mouse choroidal vascular atrophy and RPE disorganization. *Elife.* 9:e55564. https://doi.org/10.7554/eLife.55564

Young, R.W. 1971. Shedding of discs from rod outer segments in the rhesus monkey. *J. Ultrastruct. Res.* 34:190–203. https://doi.org/10.1016/s0022-5320(71)90014-1

Yu, C., E.M. Lad, R. Mathew, N. Shiraki, S. Littleton, Y. Chen, J. Hou, K. Schlepckow, S. Degan, L. Chew, et al. 2024. Microglia at sites of atrophy restrict the progression of retinal degeneration via galectin-3 and Trem2. *J. Exp. Med.* 221:e20231011. https://doi.org/10.1084/jem.20231011

Zhao, R., N. Diop-Bove, M. Visentin, and I.D. Goldman. 2011. Mechanisms of membrane transport of folates into cells and across epithelia. *Annu. Rev. Nutr.* 31:177–201. https://doi.org/10.1146/annurev-nutr-072610-145133

Zheng, Y., and L.C. Cantley. 2019. Toward a better understanding of folate metabolism in health and disease. *J. Exp. Med.* 216:253–266. https://doi.org/10.1084/jem.20181965

JEM

Supplemental material

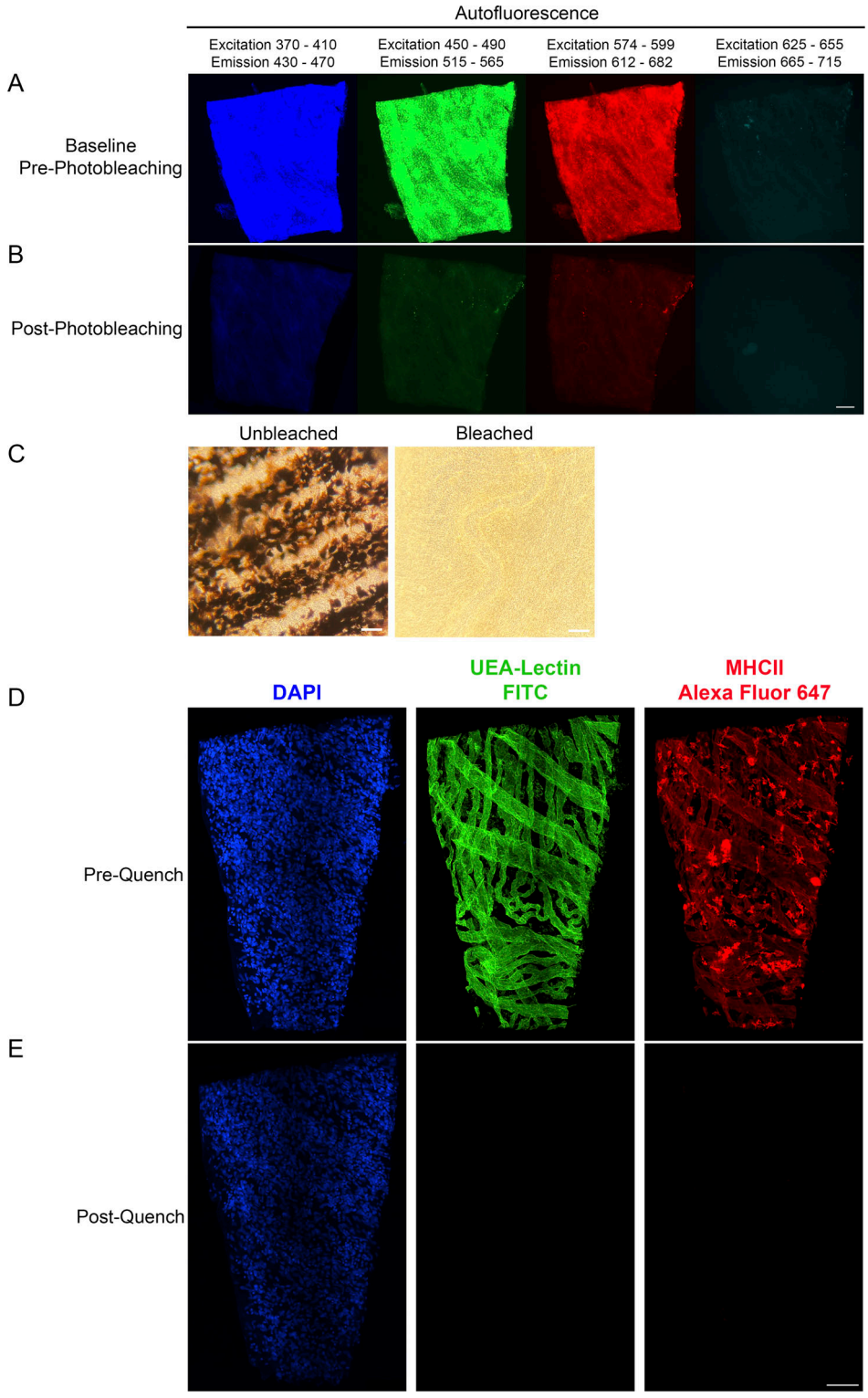

Figure S1. **Autofluorescence, pigment, and fluorophore bleaching for 3D multiplex immunofluorescence of human choroid. (A and B)** Autofluorescence in the same piece of human choroid before and after photobleaching. The same acquisition settings were used for both rounds of imaging. Channel excitation and emission are listed. Scale bar = 100 µm. **(A)** Baseline autofluorescence prior to photobleaching. Note the extreme autofluorescence in the lower wavelength channels (blue, green, and red). **(B)** Autofluorescence after two 1-h rounds of photobleaching with white LED lights followed by one 2-h round of photobleaching with 365-nm ultraviolet light. **(C)** Representative examples of pigmentation before and after photobleaching. Different pieces of choroidal tissue from the same donor are shown. Scale bars = 100 µm. **(D and E)** Immunofluorescence in the same piece of human choroid before and after photobleaching. Choroid stained with Hoechst, UEA-lectin conjugated to FITC, and anti-MHCII conjugated to Alexa Fluor 647 was imaged, photobleached, and then imaged again. The same image acquisition settings were used. Scale bar = 100 µm. **(D)** Baseline immunofluorescence before photobleaching. **(E)** Immunofluorescence after photobleaching.

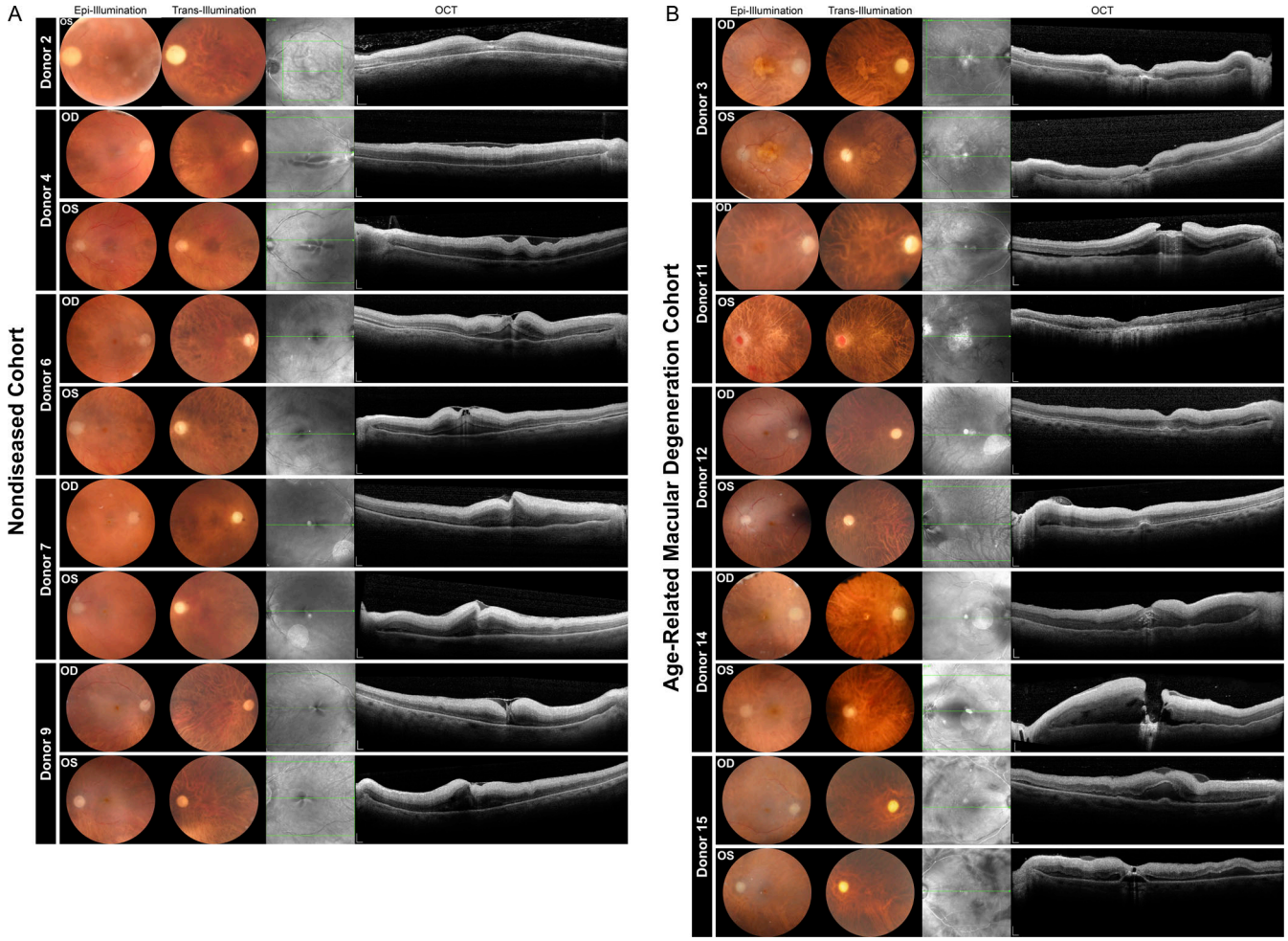

Figure S2. **Ex vivo color fundus and optical coherence tomography imaging of donor eyes. (A)** Nondiseased cohort (*n* = 9 eyes). **(B)** AMD cohort (*n* = 10 eyes). Epi-illumination refers to light source positioned superiorly. Trans-Illumination refers to light source positioned inferiorly. Scale bars = 200 µm.

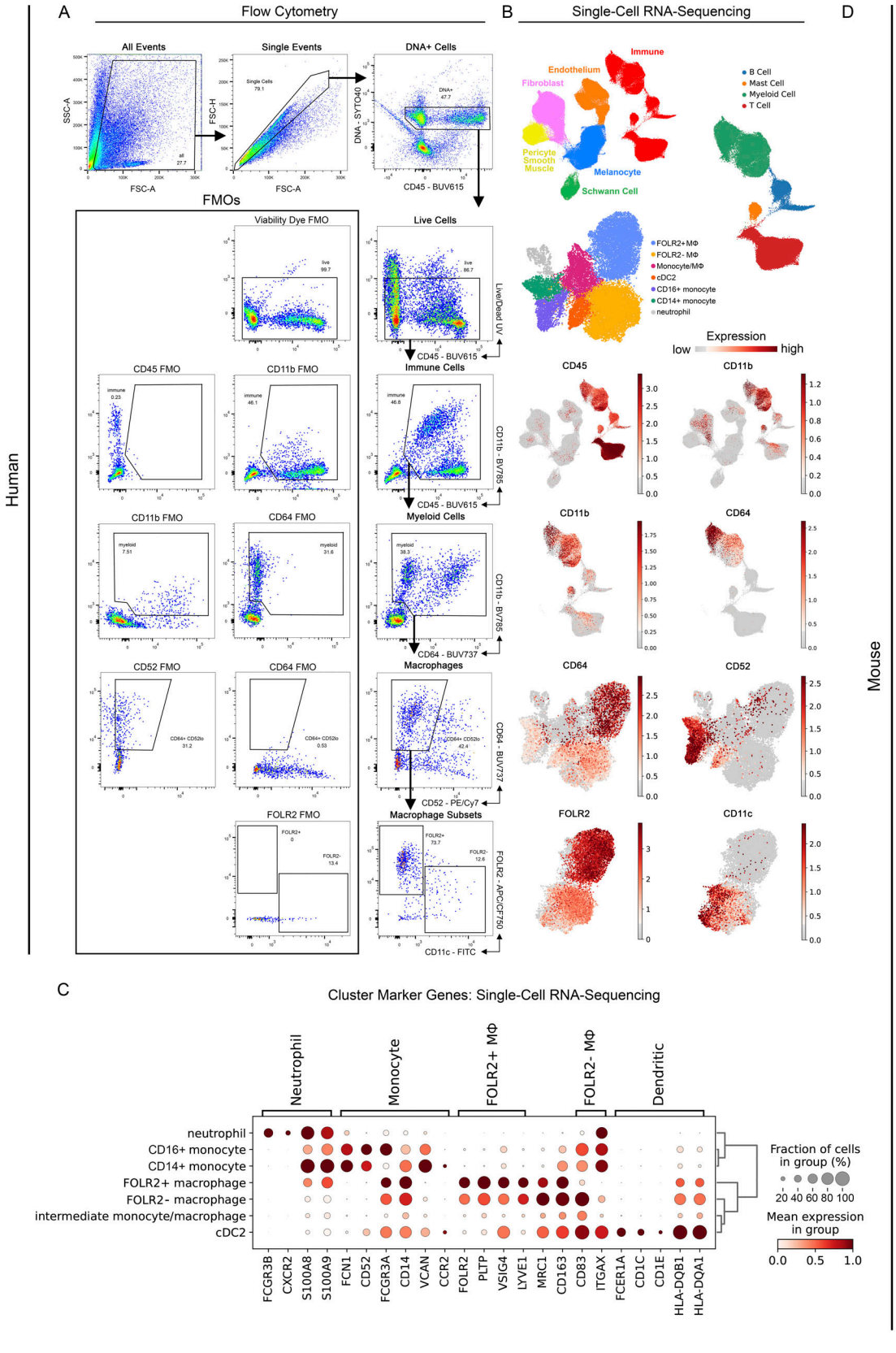

Figure S3. **scRNA-seq myeloid marker genes and flow cytometry gating schemes for human and mouse choroidal digests. (A)** Human flow cytometry gating scheme. Boxed area shows fluorescence minus one (FMO) controls for the respective gating steps. **(B)** scRNA-seq representation of the human flow cytometry gating scheme showing RNA expression of the flow cytometry target antigens for each gating step. **(C)** Marker genes for myeloid clusters from human choroid scRNA-seq. **(D)** Mouse choroid flow cytometry gating scheme. MΦ, macrophage.

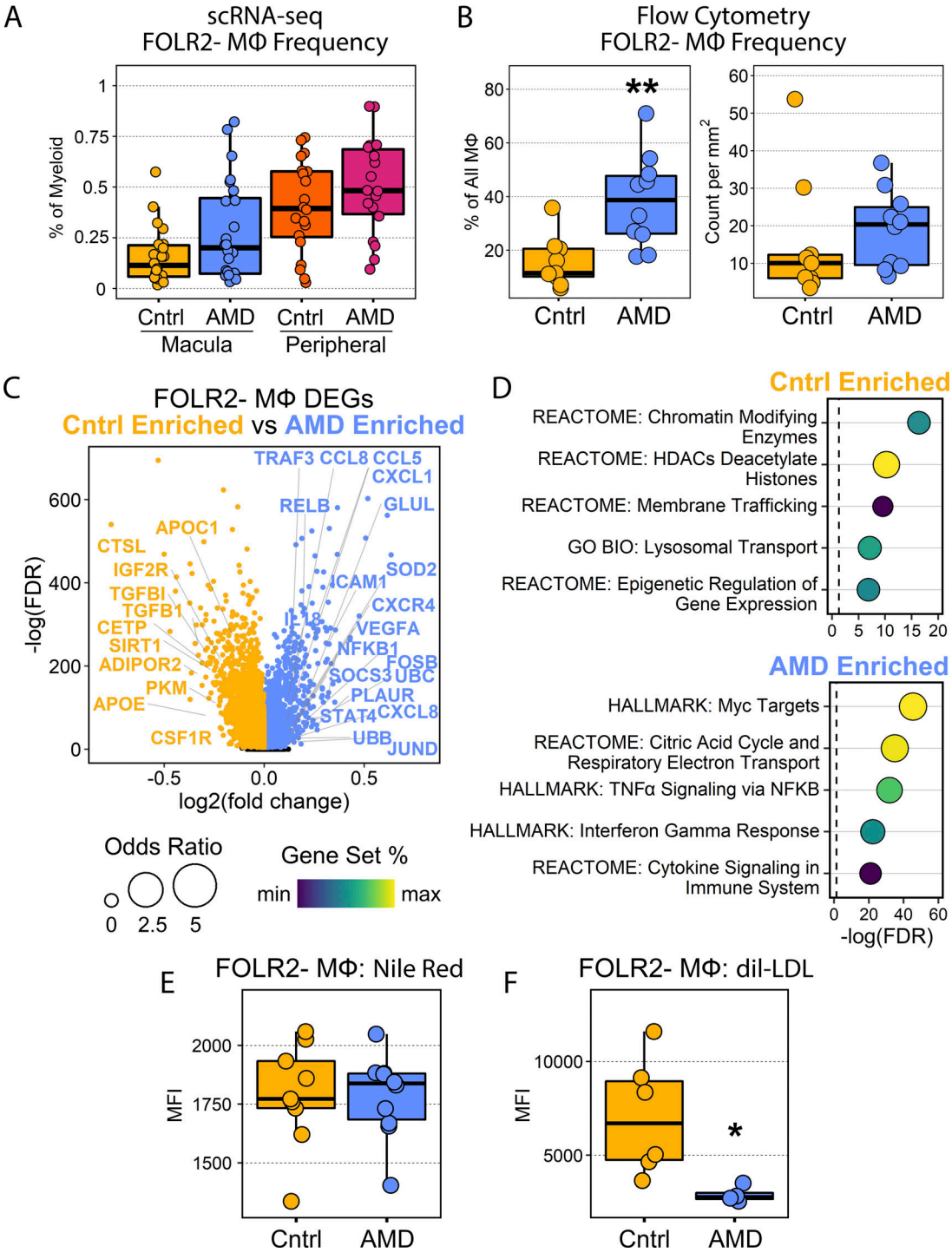

Figure S4. **Analyses of FOLR2⁻ choroidal macrophages in age-related macular degeneration. (A)** Frequency of FOLR2⁻ macrophages in scRNA-seq data relative to all myeloid cells. Nondiseased (Cntrl) macula (n = 22), AMD macula (n = 24), nondiseased peripheral (n = 20), and AMD peripheral (n = 18). Sample sizes represent unique donors by location and disease group. One-way ANOVA with Holm–Sidak correction. **(B)** Frequency of FOLR2⁻ macrophages (MΦ) relative to all macrophages from flow cytometry (left) and absolute counts of FOLR2⁻ macrophages per mm² of choroidal tissue from flow cytometry (right). Sample sizes are individual eyes. Student's t test. **(C)** Volcano plot of differentially expressed genes (DEGs) in AMD versus nondiseased macular FOLR2⁻ macrophages from scRNA-seq data. Blue = genes upregulated in AMD. Yellow = genes upregulated in nondiseased. **(D)** GSEA of DEGs from C showing selected pathways. Dashed lines represent significance cutoffs. **(E)** Flow cytometry MFI of Nile red staining in FOLR2⁻ macrophages from nondiseased (n = 9 eyes) and AMD (n = 8 eyes) donors. Student's t test. **(F)** Flow cytometry MFI of dil-LDL staining in FOLR2⁻ macrophages from nondiseased (n = 6 eyes) and AMD (n = 4 eyes) choroids. Student's t test. *P ≤ 0.05; **P ≤ 0.01. MFI; mean fluorescent intensity.

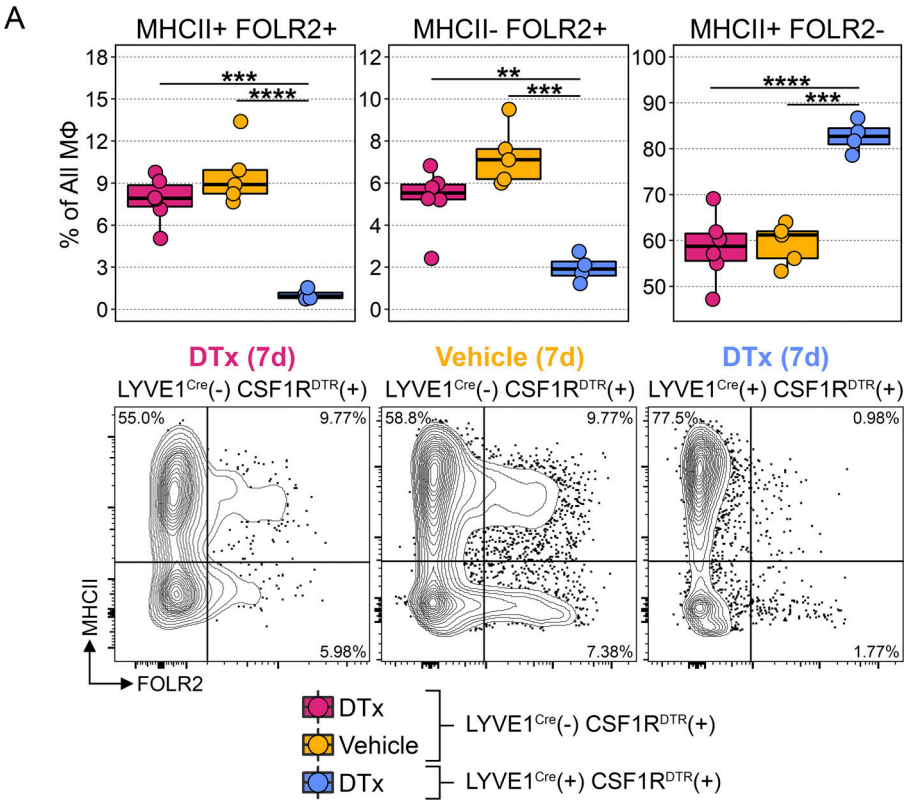

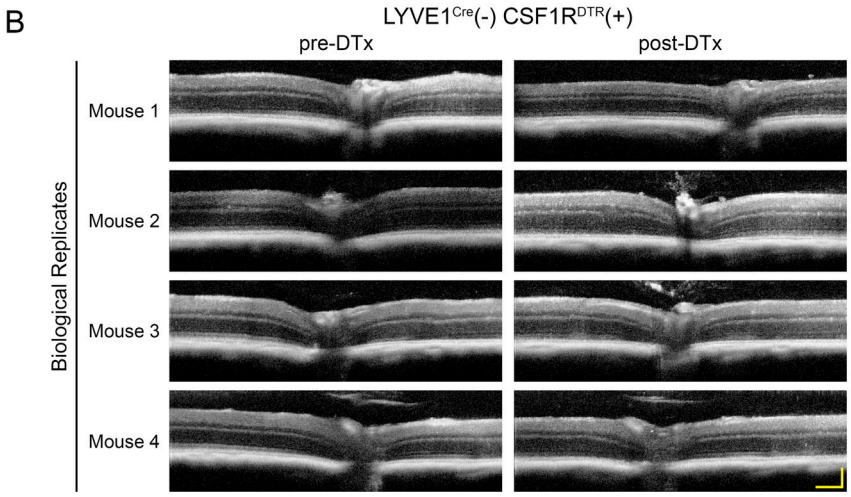

Figure S5. **Diphtheria toxin control studies. (A)** Flow cytometry from digested mouse choroids in LYVE1$^{Cre(-)}$ × CSF1R$^{DTR(+)}$ mice treated with either vehicle (yellow) or diphtheria toxin (DTx; magenta) compared with LYVE1$^{Cre(+)}$ × CSF1R$^{DTR(+)}$ mice treated with DTx (blue). Vehicle-treated LYVE1$^{Cre(-)}$ × CSF1R$^{DTR(+)}$ control mice and DTx-treated LYVE1$^{Cre(+)}$ × CSF1R$^{DTR(+)}$ depletion mice are the same cohorts from Fig. 6, C–H. DTx-treated LYVE1$^{Cre(-)}$ × CSF1R$^{DTR(+)}$ mice are an additional control cohort under the same experimental conditions. All mice were 1 mo old and treatments were for seven consecutive days (7 days) before and after laser CNV. Box plots show the frequencies of macrophage (MΦ) subsets (MHCII^{+}FOLR2^{+}, MHCII^{-}FOLR2^{+}, and MHCII^{+}FOLR2^{-}) relative to all macrophages for each of the three experimental groups. Flow cytometry plots are pre-gated on macrophages and show the macrophage subsets. One-way ANOVA with Holm–Sidak correction. ** <0.01; *** <0.001; **** <0.0001. **(B)** OCT of LYVE1$^{Cre(-)}$ × CSF1R$^{DTR(+)}$ mice before and after treatment with DTx for seven consecutive days. Four independent biological replicates. The same area of the optic nerve head is shown for the before and after DTx images. Scale bar = 100 µm.

Provided online are Table S1 and Table S2. Table S1 shows the ocular donor characteristics. Table S2 shows the ex vivo ocular imaging results.